Department of Physics and Astronomy
University of Canterbury
Christchurch, New Zealand

The population of unresolved pulsars explanation of the Galactic Center excess

Harrison Ploeg

Supervisor: Dr. Chris Gordon

Master of Science in Physics

2017

Acknowledgements

I would like to thank Dr. Chris Gordon for taking the time to supervise this MSc project and for his extremely helpful discussion and suggestions. I would also like to thank Dr. Oscar Macias for providing the point source detection threshold data in a form which was of use for this work.

Abstract

It has been suggested that a population of unresolved millisecond pulsars (MSPs) could explain the observed Galactic Center Excess (GCE). However, it has been claimed that, based on the luminosity distribution of observed MSPs, many would already have been resolved. In this work, gamma-ray MSPs detected by the Fermi Large Area Telescope (Fermi-LAT) and the GCE data are used to constrain the luminosity function through the use of a Markov chain Monte Carlo (MCMC) algorithm. The results indicate that it is indeed possible that a population of unresolved MSPs with the same luminosity distribution as those observed are the source of the GCE and that it would require further improvements in sensitivity for these to be resolved.

Contents

List of Figures

List of Tables

Chapter 1

Introduction

An excess of gamma radiation of unknown origin has been detected in Fermi Gamma-Ray Large Area Telescope (Fermi-LAT) data extending $\sim 10^\circ$ from the direction of the Galactic Center [1–9]. The source of this Galactic Center Excess (GCE) was thought to be the self-annihilation of Weakly Interacting Massive Particles (WIMPs) due to the location and spectrum of the emission. A less exotic possibility is that there is a large population of unresolved point sources emitting gamma-rays which are distributed according to the radial power law $\rho(r) \propto r^{-2.4}$ where r is distance from the Galactic Center. More recent work has indicated that the GCE has a component which is not spherically symmetric [10] and the GCE appears to be spatially correlated with the X-shaped structure in the Galactic bulge and the nuclear stellar bulge [11]. This supports the hypothesis that the GCE originates from a population of unresolved point sources rather than dark matter. Due to their similar spectra, two possible sources are millisecond pulsars (MSPs) [3, 5, 12] or young pulsars [13]. It has been claimed, however, that if MSPs with the same luminosity distribution as those observed were the source of the GCE many would already have been detected [14–16].

In this work the GCE and MSPs detected in Fermi-LAT data are used to evaluate the luminosity distribution of MSPs. This is done for two models of the bulge population of MSPs, one where the GCE is assumed to be emitted from MSPs which have a spherically symmetric distribution, and another for the case where the GCE is associated with the X-shaped structure. In Chapter 2 the Bayesian Markov chain Monte Carlo (MCMC) based approach to the problem is described as well as the method used to model populations of MSPs and the GCE. The results are presented in Chapter 3. These results are discussed in Chapter 4 and conclusions are given in Chapter 5. The data used is shown in the Appendix. The remainder of this chapter provides more background on the GCE and MSPs.

1.1 The Galactic Center Gamma-Ray Excess

The spectral peak of the GCE occurs at $\sim$ 2 GeV and the maximum intensity is located in the direction of the Galactic Center where there is expected to be a high density of dark matter. Based on this it has been suggested that the excess is caused by the self-annihilation of dark matter, with a Navarro-Frenk-White (NFW) like density profile [4]:

$$\rho(r) = \frac{\rho_s}{(r/r_s)^{\gamma}\,(1+(r/r_s)^{\alpha})^{(\beta-\gamma)/\alpha}} \tag{1.1}$$

where $r_s = 23.1$ kpc, $\alpha = 1$, and $\beta = 3$. This distribution is the density of dark matter at distance r. An inner slope $\gamma = 1.2$ fits the data well with the signal produced at a point on a line of sight proportional to $\rho(r)^2$ [4]. Gordon and Macias [4] also found that WIMPs of mass 20 to 60 GeV annihilating to a pair of leptons $\tau^+\tau^-$ and quarks $b\bar{b}$ fits the data.

In addition to the work of Macias et al. [11] on the X-shaped bulge, recent studies [17, 18] have provided further support for the possibility that the GCE is entirely caused by a population of point sources. Bartels et al. [18] claim to have detected the clustering of photons that would be expected to occur if the excess emission was from a population of dim sources. Lee et al. [17] uses non-Poissonian photon statistics to similarly suggest that a population of unresolved sources produces the excess rather than the smooth NFW profile of dark matter. However, these studies may not have found evidence of a point source population below the detection threshold but could instead be simply detecting variations in the gamma-ray flux associated with the small scale structure of a mismodeled diffuse background [19].

1.2 Millisecond Pulsars

The gamma-ray spectra of MSPs are similar to that of the GCE [5] suggesting the possibility that a population distributed throughout the central bulge of the Milky Way, but not luminous enough to be detected, could largely produce the observed excess. MSPs are pulsars observed by Fermi-LAT as gamma-ray pulsations with periods on the order of milliseconds.

1.2.1 Pulsars

Pulsars are rapidly rotating neutron stars with strong magnetic fields, they emit a beam of radiation along the magnetic axis that can be observed when that beam is pointing in the direction of the observer [20]. The periodic pulsations that result allow the rotational period P of the neutron star to be measured, as well as the rate of change of the period $\dot{P}$. This data is shown for pulsars in the ATNF catalog [21] in Fig. 1.1. From this figure, it can be seen that MSPs spin down extremely slowly in comparison to typical pulsars. The measured $\dot{P}$ can be affected by the proper motion of the pulsar so $\dot{P}$ was used with corrections for this Shklovskii effect where available. The locations of ATNF pulsars in galactic coordinates are shown in Fig. 1.2.

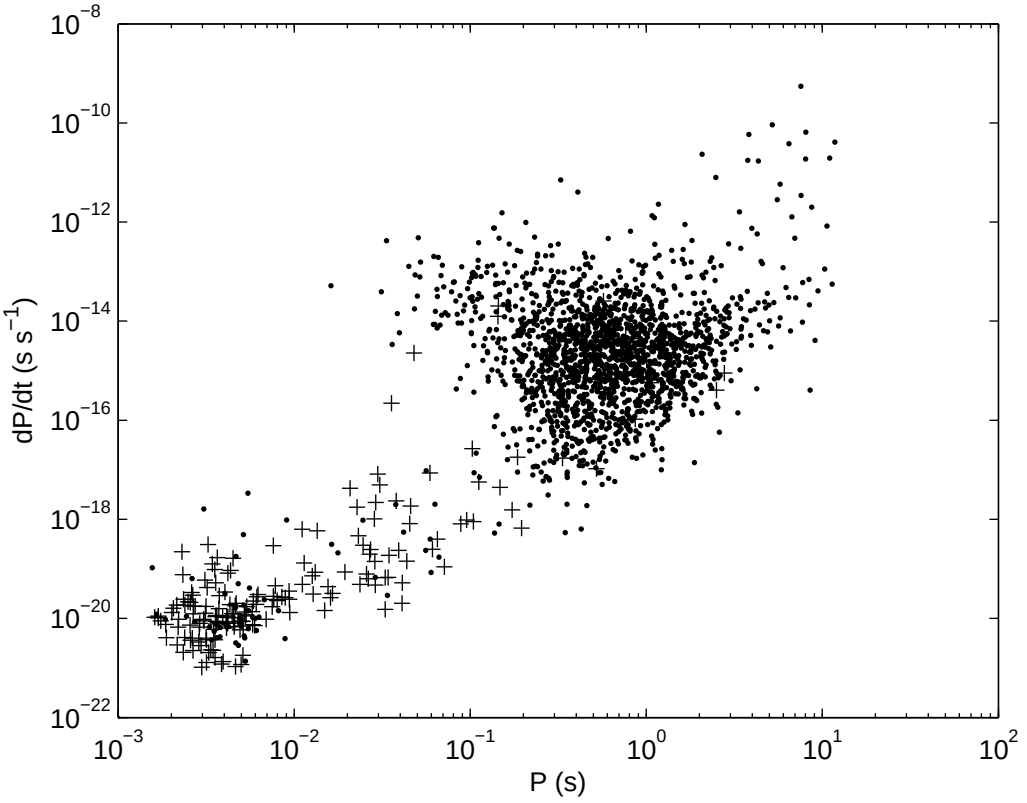

Figure 1.1: The periods and period derivatives of pulsars from the ATNF pulsar catalog [21]. Crosses are pulsars with binary companions.

From measurements of P and $\dot{P}$ other properties of a pulsar can be derived. One of these is the rate at which a pulsar is losing rotational kinetic energy [22]:

$$\dot{E} = 4\pi^2 I \dot{P} P^{-3} \tag{1.2}$$

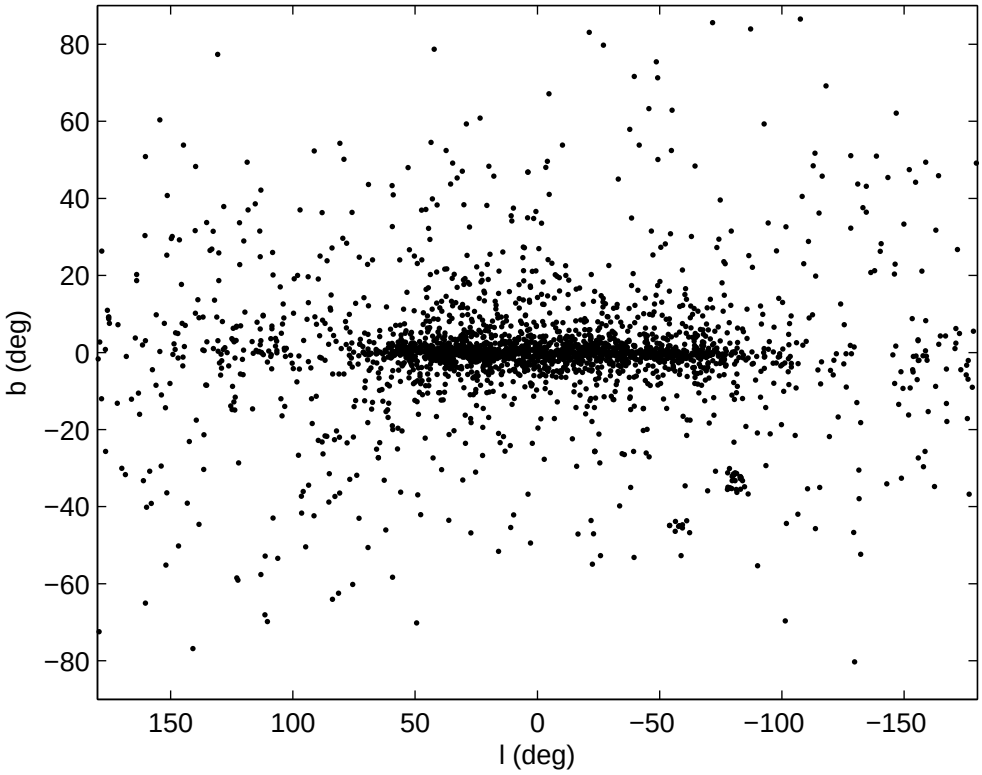

Figure 1.2: The positions in galactic coordinates of pulsars from the ATNF pulsar catalog [21].

where $I = 10^{45}$ g cm^2. It is this loss of energy which powers the emission of radiation.

The characteristic age of a pulsar is:

$$\tau_c = \frac{P}{2\dot{P}} \tag{1.3}$$

This gives an estimate for the age of the pulsar that may be accurate to within a factor of 2 or 3 [23]. Fig. 1.3 plots P against τ_c for ATNF pulsars. It can be seen that MSPs tend to be significantly older than other pulsars, with characteristic ages of on the order of several billion years instead of the 10^6 to 10^8 years typical for other pulsars.

Assuming the magnetic axis is orthogonal to the rotation axis, the magnetic field at the surface of a pulsar is [20]:

$$B_{\rm S} = \frac{1}{2\pi R_{\rm NS}^3}\sqrt{1.5Ic^3P\dot{P}} \tag{1.4}$$

where c is the speed of light in a vacuum and $R_{\rm NS} = 10$ km is assumed to be the radius of a neutron star. Fig. 1.4 plots P against $B_{\rm S}$ for the ATNF pulsars. From

this it is clear that MSPs have magnetic fields that are considerably weaker than other pulsars, by a factor of around 10^4.

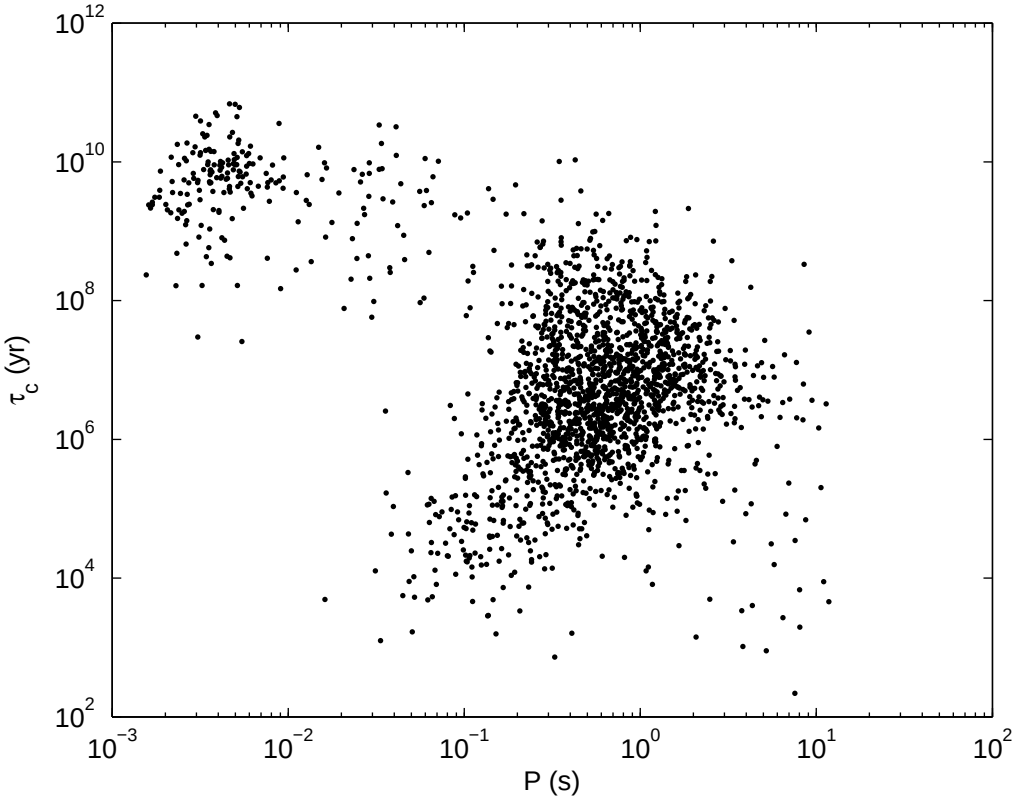

Figure 1.3: The periods and characteristic ages of pulsars from the ATNF pulsar catalog [21].

An estimate of distance can be made using the dispersion measure. This is due to the fact that different radio frequencies will arrive at different times as a result of the interstellar medium. For a single pulse of radiation from the pulsar, lower frequencies will arrive later than higher ones, and this delay is dependant on distance. The dispersion measure can be found from [24]:

$$\Delta t = 4.15 \text{ ms} \left(\left(\frac{\nu_{\text{lo}}}{\text{GHz}} \right)^{-2} - \left(\frac{\nu_{\text{hi}}}{\text{GHz}} \right)^{-2} \right) \left(\frac{\text{DM}}{\text{cm}^{-3} \text{ pc}} \right) \tag{1.5}$$

where Δt is the delay between the arrival of a high frequency ν_{hi} and a low frequency ν_{lo} and DM is the dispersion measure. Then the distance d can be found by solving the following for d [24]:

$$\text{DM} = \int_0^d n_{\text{e}} \, \text{d}l \tag{1.6}$$

where n_{e} is the density of free electrons. This then requires a model of the dis-

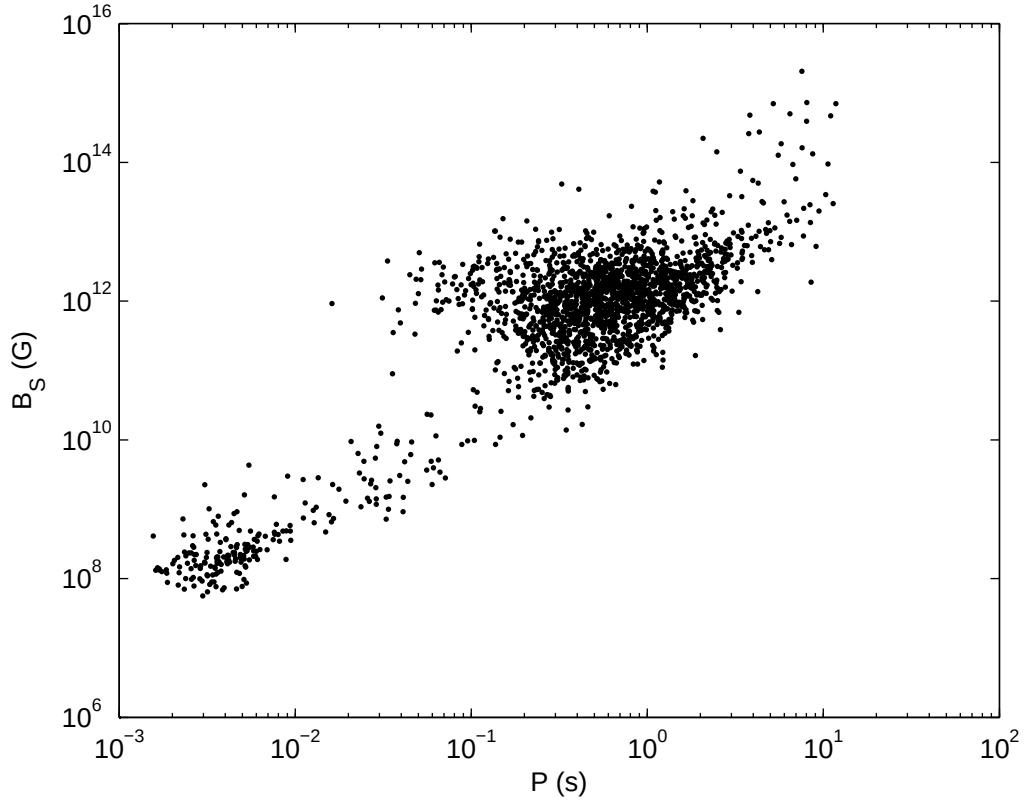

Figure 1.4: The periods and magnetic field at the surface of pulsars from the ATNF pulsar catalog [21].

tribution of free electrons, such as the NE2001 model [25]. There is the potential, however, for large systematic uncertainties in these distance estimates.

1.2.2 Neutron Stars

Neutron stars are stars with small radii of $\sim$ 10 km, masses of on the order of $1.5M_\odot$ and therefore extremely high densities of $\sim 10^{15}$ g cm^{-3} [23, 26, 27]. They are formed in supernovae which occur when electron degeneracy pressure fails to prevent the iron core of a massive star ($M \gtrsim 8M_\odot$) from gravitational collapse, causing a shock which blows away the remaining material [27].

Potekhin [27] divides the structure of a neutron star into several regions. The atmosphere is an extremely thin layer of plasma which emits thermal radiation. This layer has a thickness ranging from millimeters to tens of centimeters depending on temperature. The atmosphere has an effective temperature of $\sim 10^6$ K with a density ranging $\sim 10^{-4}$ to $\sim 10^6$ g cm^{-3} at the bottom depending on various factors such as the magnetic field. The second region described by Potekhin [27] is the ocean, which is largely composed of nuclei and electrons. The outer crust is similar

to the ocean but fully ionized. The inner crust, which has densities of greater than $\sim 5 \times 10^{11}$ g cm^{-3}, is composed of a neutron superfluid as well as heavy nuclei rich in neutrons which form a lattice along with degenerate electrons. It is relatively thick at around $1 - 2$ km. The mantle consists also of neutron superfluid and degenerate electrons. In addition, the nuclei are likely found with various non-spherical shapes known as nuclear pasta [23]. The core, which contains almost the entire mass of the star, is divided into two components, the inner core, and the outer core. The outer core may consist of a neutron superfluid with the protons forming a superconductor as well as electrons and muons. The inner core would likely be composed of more exotic matter.

1.2.3 Formation of Millisecond Pulsars

The basic process behind the formation of an MSP is the transfer of mass and angular momentum from a binary companion to an ordinary pulsar [28]. This requires a binary system containing a massive star. The binary system must also then survive the supernova in which a pulsar is formed from core of this massive star [24]. Eventually, the binary companion will evolve into a giant, at which point it may overflow it's Roche lobe and an accretion disk will form around the pulsar. This accretion of material onto the neutron star increases it's angular momentum, spinning up the pulsar. The period will at some point reach an equilibrium $P_{\rm eq}$ which according to Tauris et al. [29] is:

$$P_{\rm eq} \approx 1.40 \text{ ms } \left(\frac{B_{\rm S}}{10^8 \text{ G}}\right)^{6/7} \left(\frac{\dot{M}}{0.1\dot{M}_{\rm Edd}}\right)^{-3/7} \left(\frac{M}{1.4M_\odot}\right)^{-5/7} \left(\frac{R_{NS}}{13 \text{ km}}\right)^{13/7} \tag{1.7}$$

where M is the mass of the neutron star, $\dot{M}$ is the rate at which mass is accreted and $\dot{M}_{\rm Edd}$ is the Eddington accretion limit [29]:

$$\dot{M}_{\rm Edd} \approx 3.0 \times 10^{-8} M_\odot \text{ yr}^{-1} \left(\frac{R_{NS}}{13 \text{ km}}\right) \left(\frac{1.3}{1+X}\right) \tag{1.8}$$

where X is the hydrogen mass fraction. The accretion rate cannot be higher than this limit as this is where the force of gravitation towards the neutron star is balanced by the outward force caused by radiation pressure. This radiation occurs because friction is heating the material being accreted onto the neutron star, generating X-rays [24].

Tauris et al. [29] also show that at the equilibrium period $P_{\rm eq}$, the total mass of the material accreted is:

$$\Delta M_{\rm eq} \approx 0.22 M_\odot \left(\frac{M}{M_\odot}\right)^{1/3} \left(\frac{P_{\rm eq}}{1\ {\rm ms}}\right)^{-4/3} \tag{1.9}$$

This relationship is shown in Fig. 1.5 for $M = 1.5 M_\odot$.

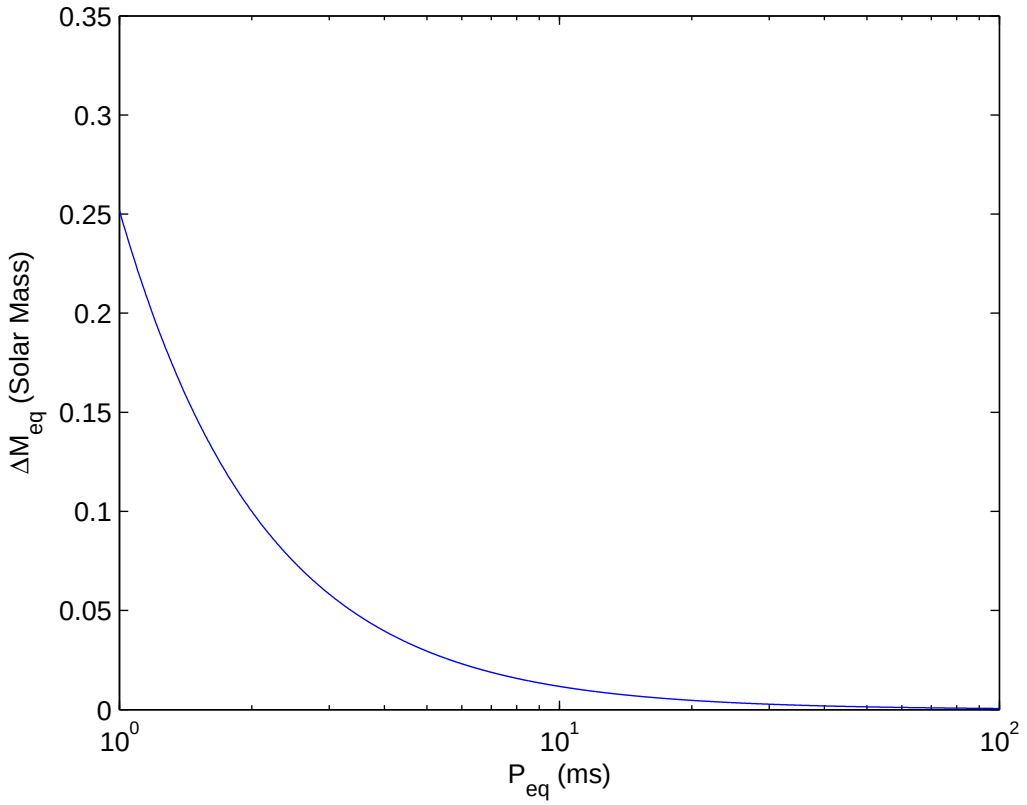

Figure 1.5: The accreted mass necessary to spin up a pulsar to the equilibrium period $P_{\rm eq}$. $M = 1.5 M_\odot$ was assumed.

A pulsar spun up in this fashion by the accretion of matter from a binary companion is said to have been recycled. As can be seen in Fig. 1.1, MSPs are indeed very likely to be found in binary systems, whereas other pulsars only very rarely have a companion. There are, however, a number which appear to be isolated. Some of these may have been Black Widows, where, due to a small orbit and low mass, ablation of the companion by the pulsar wind has entirely destroyed it [30]. Another possibility is that the binary systems did not survive when a second supernova occurred [24].

Chapter 2

Method

Table A.3 contains a list of 71 MSPs found within the Fermi Large Area Telescope third source catalog (3FGL) [31]. The table presents the position of each MSP in galactic coordinates, the gamma-ray flux in the 100 MeV to 100 GeV energy range, spectral parameters, and distance estimates. These MSPs were found by searching the Australia Telescope National Facility (ATNF) pulsar catalog [21] for pulsars with periods of less than 10 milliseconds and which were not associated with globular clusters. These MSPs were then used if a gamma-ray source recorded as being associated with the pulsar was found in the 3FGL catalog. A small number of additional MSPs were identified through the use of an online list[1] and also found in the 3FGL catalog.

2.1 Modelling a Population of Millisecond Pulsars

To simulate a GCE and population of observed MSPs to compare with data, the underlying population of MSPs must be modelled. This requires spatial and luminosity models, and for the MSPs around the Galactic Center that may be responsible for the excess, a distribution of spectra.

Two different luminosity functions were considered, a lognormal distribution (also used by Hooper and Mohlabeng [14]) and a simple power law. The lognormal distribution is one in which the logarithm (of any base) of luminosity is normally distributed, it's probability density function is:

[1] https://confluence.slac.stanford.edu/display/GLAMCOG/Public+List+of+LAT-Detected+Gamma-Ray+Pulsars

$$p(L) = \frac{1}{\sigma_L L\sqrt{2\pi}} \exp\left(\frac{-(\ln(L) - \ln(L_{\text{med}}))^2}{2\sigma_L^2}\right) \tag{2.1}$$

where L is luminosity, L_{med} is the median luminosity, and $\ln(L_{\text{med}})$ and σ_L are the mean and standard deviation of the normal distribution in $\ln(L)$. This distribution is defined for $(0, \infty)$, but the integral is finite. The simple power law, defined between L_{min} and L_{max} with parameter α, has the following probability distribution:

$$p(L) = \begin{cases} \frac{\alpha-1}{L_{\text{min}}^{1-\alpha} - L_{\text{max}}^{1-\alpha}} L^{-\alpha}, & \alpha \neq 1 \\ ((\ln(L_{\text{max}}) - \ln(L_{\text{min}}))L)^{-1}, & \alpha = 1 \end{cases} \tag{2.2}$$

If x, y, and z define the position of an MSP in a Cartesian coordinate system with the origin at the Galactic Center, this position can be converted to a location in galactic coordinates. Galactic coordinates define a direction by longitude l and latitude b, where $(l, b) = (0, 0)$ is the direction of the Galactic Center. If the position of the sun is chosen to be $(x, y, z) = (-r_\odot, 0, 0)$ ($r_\odot = 8.25$ kpc was assumed), the positions of MSPs in Cartesian coordinates are related to l, b and distance d by:

$$\begin{aligned} x &= d\cos(l)\cos(b) - r_\odot \\ y &= d\sin(l)\cos(b) \\ z &= d\sin(b) \end{aligned} \tag{2.3}$$

The spatial distribution of MSPs was divided into two components. One of these components models a population of MSPs scattered throughout the Milky Way disk according to the following density distribution:

$$\rho_{\text{disk}}(r, z, N_{\text{disk}}) = \frac{N_{\text{disk}}}{4\pi\sigma_r^2\sigma_z} \exp\left(-r^2/2\sigma_r^2\right) \exp(-|z|/\sigma_z) \tag{2.4}$$

where $r = \sqrt{x^2 + y^2}$, N_{disk} is the total number of MSPs in the disk, and σ_r and σ_z are scale parameters. An example distribution of disk MSPs is shown in Fig. 2.1.

The circular symmetry of the disk model around the z-axis means a natural way to generate random samples would be to do so in cylindrical coordinates. To sample a random point from this spatial model, $|z|$ is drawn from an exponential distribution with scale parameter σ_z, then z is assigned either $|z|$ or $-|z|$ each with probability 0.5. A value for θ is then drawn from a uniform distribution on the interval $[0, 2\pi)$. Finally, r is randomly drawn from the following probability distribution function:

$$f(r) = \frac{1}{\sigma_r^2} \exp\left(-r^2/2\sigma_r^2\right) r \tag{2.5}$$

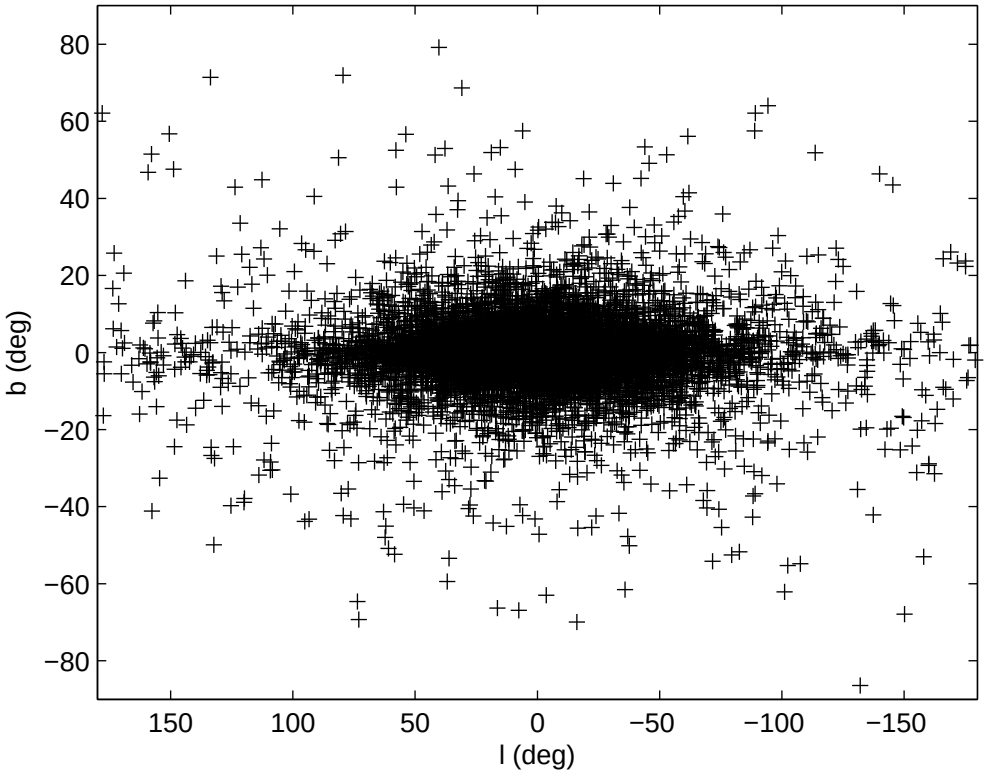

Figure 2.1: Simulated spatial distribution of disk MSPs using $\sigma_r = 5$ kpc, $\sigma_z = 0.75$ kpc.

The factor of r is related to the volume element $\mathrm{d}V = r\,\mathrm{d}r\,\mathrm{d}z\,\mathrm{d}\theta$. A simple way to sample the distribution in Eq. (2.5) is to perform a transformation on uniformly distributed random numbers [32]. Let $f(u)$ define some normalized probability density function, with it's integral $F(u)$ the cumulative probability distribution, then if v is drawn from a uniform distribution on the interval $[0, 1]$, we can transform it using the following:

$$u = F^{-1}(v) \tag{2.6}$$

So in the case of the disk distribution of r, by drawing v from $[0, 1)$:

$$r = \sqrt{2}\sigma_r \sqrt{\ln\left(\frac{1}{1-v}\right)} \tag{2.7}$$

r and θ can be converted to Cartesian coordinates by:

$$x = r\cos(\theta)$$
$$y = r\sin(\theta) \tag{2.8}$$

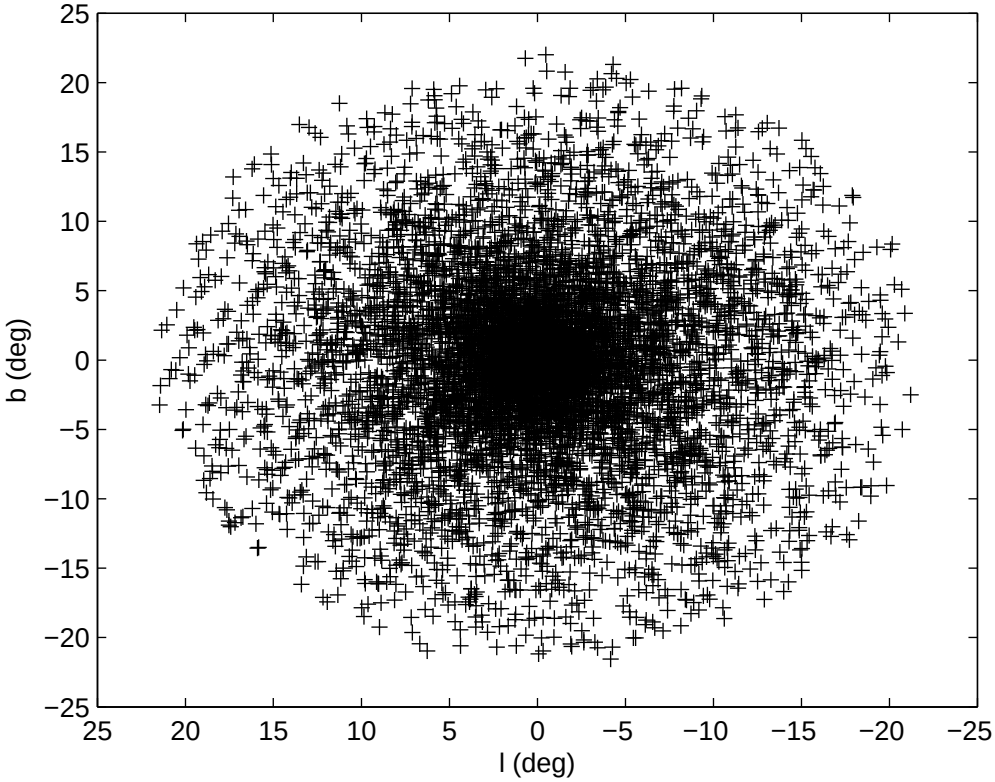

Figure 2.2: Simulated spatial distribution of spherically symmetric bulge MSPs with $r_{\rm bulge} = 3.1$ kpc.

The second component of the spatial distribution models the bulge population of MSPs potentially contributing to the GCE. This density distribution is:

$$\rho_{\rm bulge}(r, N_{\rm bulge}) = \frac{3N_{\rm bulge}}{20\pi r_{\rm bulge}^{0.6}} r^{-2.4}, \quad 0 \leq r < r_{\rm bulge} \tag{2.9}$$

where $r = \sqrt{x^2 + y^2 + z^2}$, $N_{\rm bulge}$ is the total number of bulge MSPs and $r_{\rm bulge}$ is the maximum extent of the bulge. This distribution, shown in Fig. 2.2, is spherically symmetric, so it was sampled randomly using spherical coordinates where:

$$
\begin{aligned}
x &= r\cos(\theta)\sin(\phi) \\
y &= r\sin(\theta)\sin(\phi) \\
z &= r\cos(\phi)
\end{aligned}
\tag{2.10}
$$

and for which the volume element is $\mathrm{d}V = r^2\sin(\phi)\,\mathrm{d}r\,\mathrm{d}\theta\,\mathrm{d}\phi$. The density does not depend on θ so it is uniformly distributed on $[0, 2\pi)$. The radial coordinate r is drawn from the following distribution:

$$
f(r) = \frac{3}{5r_{bulge}^{0.6}} r^{-0.4}, \quad 0 \leq r < r_{\mathrm{bulge}} \tag{2.11}
$$

which by Eq. (2.6) involves drawing a random number v from $[0, 1)$ and using the transformation:

$$
r = r_{\mathrm{bulge}} v^{5/3} \tag{2.12}
$$

Finally, we draw ϕ from:

$$
f(\phi) = \sin(\phi), \quad 0 \leq \phi < \pi \tag{2.13}
$$

which, again by Eq. (2.6), can be done using:

$$
\phi = \cos^{-1}(1 - 2v) \tag{2.14}
$$

In addition to the spherically symmetric bulge model, an alternative model in which the bulge is X-shaped [11] was also used. In this case, the spatial distribution is the same, but accepting only points randomly generated inside the projected X-shaped structure in galactic coordinates. This X-shaped bulge distribution is shown in Fig. 2.3.

Once the positions and luminosities of a population of MSPs (in both the disk and bulge) were simulated, an observed population could be found by applying a detection threshold based on the flux of each MSP. The relationship between flux F, luminosity L and distance d is:

$$
F = \frac{L}{4\pi d^2} \tag{2.15}
$$

A resolved MSP is one for which $F \geq F_{\mathrm{th}}$ where F_{th} is the threshold flux. As in the work by Hooper and Mohlabeng [14], the threshold did not solely depend on location in galactic coordinates, F_{th} was instead drawn from a lognormal distribution for each

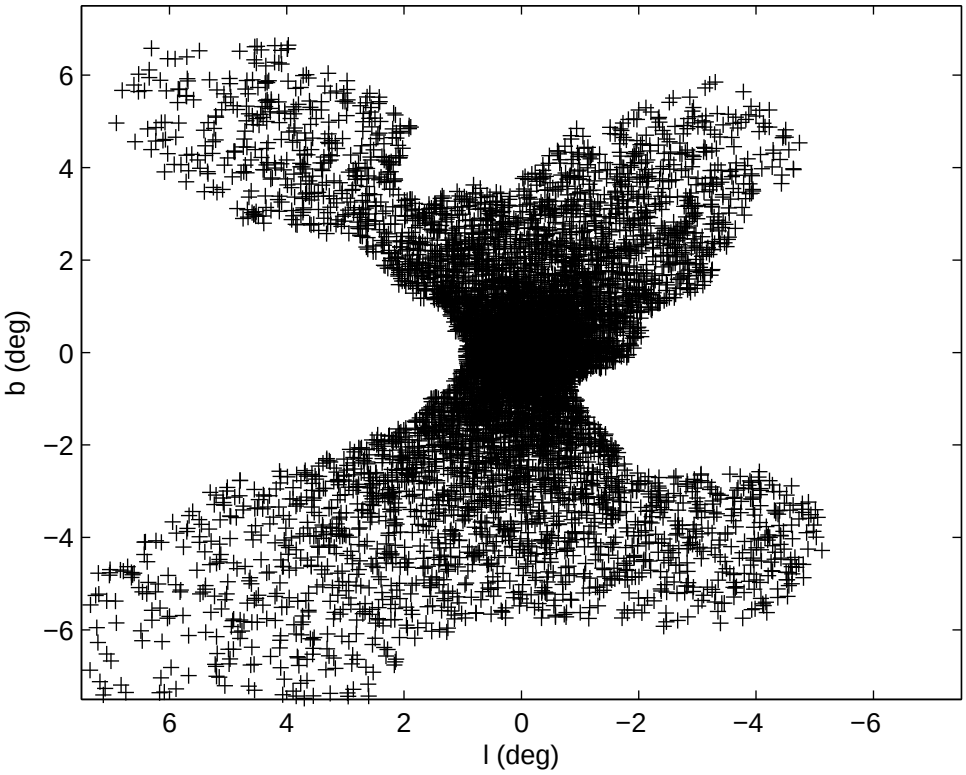

Figure 2.3: Simulated spatial distribution of MSPs in X-shaped bulge with $r_{\text{bulge}} = 1.5$ kpc.

simulated MSP:

$$p(F_{\text{th}}) = \frac{1}{\sigma_{\text{th}} F_{\text{th}} \sqrt{2\pi}} \exp\left(\frac{-(\ln(F_{\text{th}}) - (\mu_{\text{th}}(l,b) + K_{\text{th}}))^2}{2\sigma_{\text{th}}^2} \right) \tag{2.16}$$

where K_{th} and σ_{th} are parameters, and $\mu_{\text{th}}(l,b)$ depends on latitude and longitude. The second Fermi Large Area Telescope catalog of gamma-ray pulsars [20] included an attempt to find the detection threshold as a function of l and b by adding simulated point sources and attempting to fit the data. The natural logarithm of the threshold flux at l and b according to that catalog is $\mu_{\text{th}}(l,b)$. This flux threshold is shown in Fig. 2.4, the higher detection threshold around $b = 0°$ is caused by the galactic plane. Abdo et al. [20] point out that these reported detection thresholds are likely to be underestimates, K_{th} is included as a parameter to account for this. The purpose of drawing F_{th} from the lognormal distribution is to approximate the variation that may occur due to uncertainty in the estimated threshold, or characteristics specific to individual pulsars, such as their spectra or light curves.

To simulate the GCE, a distribution of spectra must be modelled for the bulge MSPs. In the 3FGL catalog sources were fitted with three different spectral shapes.

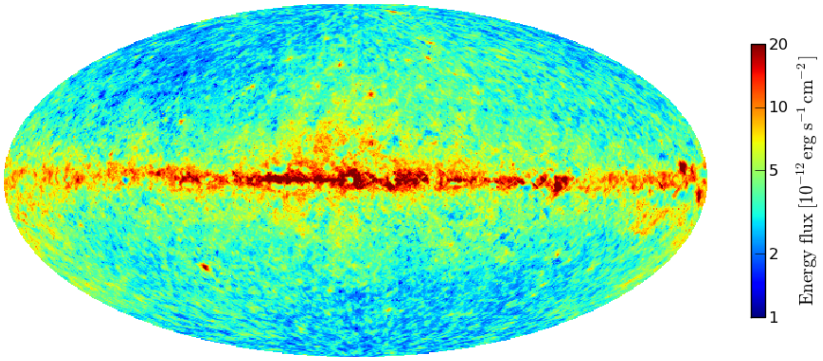

Figure 2.4: Second pulsar catalog flux detection threshold. This has been multiplied by a factor of two as the original estimates are believed to underestimate the sensitivity to point sources. This is Figure 16 from Abdo et al. [20].

One of these is a power law:

$$\frac{\mathrm{d}N}{\mathrm{d}E} \propto \left(\frac{E}{E_0}\right)^{-\Gamma} \tag{2.17}$$

The second is an exponentially cutoff power law:

$$\frac{\mathrm{d}N}{\mathrm{d}E} \propto \left(\frac{E}{E_0}\right)^{-\Gamma} \exp\left(-\frac{E}{E_{\mathrm{cut}}}\right) \tag{2.18}$$

Finally, a log parabolic spectrum was fitted for a small number of the observed MSPs:

$$\frac{\mathrm{d}N}{\mathrm{d}E} \propto \left(\frac{E}{E_0}\right)^{-\alpha-\beta\ln(E/E_0)} \tag{2.19}$$

Each simulated bulge MSPs was assigned the spectral shape and best fit parameters of a random resolved MSP as found in Table A.3. The proportionality constant was then found by requiring the energy integral over the spectrum (from 0.1 to 100 GeV) be equal to the flux:

$$F = \int_{0.1\text{ GeV}}^{100\text{ GeV}} E\frac{dN}{dE}dE \tag{2.20}$$

The simulated GCE was then the sum of the spectra of all the MSPs in the relevant region of interest. This region is the $7^\circ \times 7^\circ$ box around the galactic center in the

case of the spherically symmetric bulge, and for the X-shaped bulge it is the entire simulated bulge (which is inside a $15^\circ \times 15^\circ$ region).

2.2 Markov Chain Monte Carlo

In 2.1 a model was described which can produce a simulated population of MSPs, decide which are resolved and simulate a GCE based on the bulge MSP population. To find the parameters which may best reproduce the data, it is necessary to have a method for randomly sampling an arbitrary and potentially complex probability distribution of any number of dimensions.

The Metropolis algorithm is a Markov chain Monte Carlo (MCMC) method that attempts to generate a Markov chain of points distributed according to some probability density $p(x)$. Starting from an initial point x_0 and using some proposal distribution $q(y|x)$ which is symmetric ($q(y|x) = q(x|y)$), the standard Metropolis algorithm operates as follows at iteration t [33]:

1. Propose a new point y drawn from $q(y|x_{t-1})$
2. Calculate acceptance probability $\alpha = \min(1, \frac{p(y)}{p(x_{t-1})})$
3. Draw random number r from uniform distribution on $[0, 1)$
4. If $r < \alpha$, $x_t = y$, otherwise $x_t = x_{t-1}$

Following a large number of iterations the distribution of points in the Markov chain will converge to $p(x)$.

An inappropriate proposal distribution can cause the Markov chain to converge too slowly, requiring the use of very long chains. If, for example, the proposal distribution is too small, the algorithm will take a long time to fully explore the parameter space. If the proposal distribution is too large, the acceptance probability α may often be close to 0 and therefore the vast majority of proposal points may be rejected. To resolve this issue the adaptive Metropolis algorithm developed by Haario et al. [34] was used. The adaptive Metropolis uses a multivariate normal distribution to propose new points. The mean of this proposal distribution at iteration t is x_{t-1} with covariance matrix C_t. This covariance matrix is constructed from all previous points in the chain:

$$C_t = s_d \operatorname{cov}(x_0, \ldots, x_{t-1}) + s_d \varepsilon I_d \tag{2.21}$$

where $s_d = (2.4)^2/d$, d being the number of dimensions, ε is a small constant and $\mathrm{cov}(x_0, \ldots, x_{t-1})$ the covariance matrix of all the points in the history of the chain is:

$$\mathrm{cov}(x_0, \ldots, x_{t-1}) = \frac{1}{t-1}\left(\sum_{i=0}^{t-1} x_i x_i^T - t\bar{x}_{t-1}\bar{x}_{t-1}^T\right) \tag{2.22}$$

where $x_i x_i^T$ and $\bar{x}_{t-1}\bar{x}_{t-1}^T$ are outer products and where $\bar{x}_{t-1}$ is the mean:

$$\bar{x}_{t-1} = \frac{1}{t}\sum_{i=0}^{t-1} x_i \tag{2.23}$$

For the first t_0 iterations an initial covariance matrix for the proposal distribution is used. Since this choice of initial C_t may be quite poor, the first t_0 points in the chain included only accepted moves, this ensured that when the covariance matrix was first constructed, it was not possible that no new points had been accepted. So that those initial t_0 iterations would not have any significant effect on the covariance matrix in the long run, t_0 was chosen such that $t_0 \ll t_{\max}$, where $t_{\max}$ is the total length of the chain.

The probability distribution that was explored using this MCMC method was [33]:

$$p(\theta|y) \propto p(\theta)p(y|\theta) \tag{2.24}$$

where θ is the model parameters, y is the observed data, $p(\theta|y)$ is referred to as the posterior, $p(\theta)$ the prior on the model parameters, and $p(y|\theta) = \mathcal{L}(\theta|y)$ is the likelihood. The prior includes information about our prior beliefs about the distribution of the parameters. The likelihood is the probability of the data according to the model.

A common way to calculate the likelihood is to bin data such that n_i is the number of observations in bin i, then, using the model, calculate the expected number of observations in each bin λ_i. One way to find λ_i is by integrating the model density function over the bin. Alternatively, as that may be difficult to do efficiently, it could be estimated by sampling the model a large number of times, binning the simulated data, and normalizing to the appropriate total expected number of observations. The likelihood is then [33, 35]:

$$\begin{aligned}\mathcal{L} &= \prod_{i=1}^{N} \frac{\lambda_i^{n_i} \exp(-\lambda_i)}{n_i!} \\ &= \exp(-\lambda_{\text{tot}}) \prod_{i=1}^{N} \frac{\lambda_i^{n_i}}{n_i!}\end{aligned} \tag{2.25}$$

where N is the number of bins and $\lambda_{\text{tot}} = \sum_{i=1}^{N} \lambda_i$. With a relatively small number of observations, it is better to use an unbinned likelihood [35]. If the size of the bins is shrunk to where every n_i is either 0 or 1, then the likelihood is:

$$\mathcal{L} = \exp(-\lambda_{\text{tot}}) \prod_{i \in S} \lambda_i \tag{2.26}$$

where S is the set of all indices for bins where $n_i = 1$. If we define the average density $\rho_i = \lambda_i / V_i$ where V_i is the size of the bin (not necessarily in a 3 dimensional space), then we have:

$$\mathcal{L} \propto \exp(-\lambda_{\text{tot}}) \prod_{i \in S} \rho_i \tag{2.27}$$

If we continue to shrink the bins until they are infinitesimal in size, then:

$$\mathcal{L} \propto \exp(-\lambda_{\text{tot}}) \prod_{i=1}^{N} f(x_i) \tag{2.28}$$

where N is now the number of observations and $f(x_i)$ is the modelled density at each observation.

The parameters explored by the MCMC algorithm were:

1. The total expected number of observed MSPs λ_{res}.
2. The natural log of the ratio of disk to bulge MSPs $\ln\left(r_{\text{d/b}}\right)$.
3. Luminosity function parameters $\log_{10}(L_{\text{med}})$ and σ_L for the lognormal case, and α, $\log_{10}(L_{\text{min}})$ and $\log_{10}(L_{\text{max}})$ for the simple power law case.
4. The flux threshold distribution parameters K_{th} and σ_{th}.
5. A distance parameter for each observed MSP d_i.

λ_{res} is used as a parameter (rather than fixing it to the observed number of MSPs) because the observed number is essentially drawn from a Poisson distribution with an unknown expected value. The parameters λ_{res}, σ_{th} and all d_i were required to be

greater than 0 and σ_L was restricted to values above 0.5. A lower limit of 0.8 for σ_L is justified by Hooper and Mohlabeng [14] by considering the luminosity distribution of those MSPs with parallax distance measurements. Here, those measurements were included as priors on the distance parameters corresponding to those MSPs. The distance priors were normal distributions constructed from the measurements and their errors. Distance measurements derived from the dispersion measure were not included due to uncertainty about these estimates, instead these distance parameters were only constrained by the spatial model. Prior boundaries were also used for $\log_{10}(L_{\rm med})$, $\log_{10}(L_{\rm min})$, $\log_{10}(L_{\rm max})$ and $K_{\rm th}$, these were located in places where either the likelihood was either very low (the proposed set of parameters would be extremely unlikely to be accepted) or where the likelihood becomes insensitive to the parameter. Table 2.1 lists boundaries placed on each of the parameters, only one of these, the lower boundary on $\log_{10}(L_{\rm min})$, has an effect on the results as seen in Chapter 3 and this is discussed in Chapter 4.

Parameter	Lower Boundary	Upper Boundary
$\lambda_{\rm res}$	0.0	-
$\ln\left(r_{\rm d/b}\right)$	-	-
$K_{\rm th}$	0.0	3.9
$\sigma_{\rm th}$	0.0	2.3
d_i	0.0	-
$\log_{10}(L_{\rm med})$	30.0	38.0
σ_L	0.5	3.0
α	-20.0	20.0
$\log_{10}(L_{\rm min})$	31.0	32.0
$\log_{10}(L_{\rm max})$	32.0	38.0

Table 2.1: Boundaries used for each parameter in MCMC simulation.

For simplicity, the spatial parameters were fixed at $\sigma_r = 5$ kpc and $\sigma_z = 0.75$ kpc for the disk model, these values were chosen for consistency with previous work which tends to suggest σ_z is likely in the range $0.4-1$ and σ_r in the range $3-8$ [14, 36–38]. Markov chains were also constructed using different spatial parameters in order to estimate systematic uncertainties. For the spherically symmetric bulge model $r_{\rm bulge} = 3.1$ kpc was used for consistency with the work of Hooper and Mohlabeng [14]. For the X-shaped bulge $r_{\rm bulge} = 1.5$ kpc, this was chosen to be approximately

the same size as the X-shaped structure in galactic coordinates.

The likelihood used could be separated into two major components and written as:

$$\mathcal{L} = \mathcal{L}_{\rm GCE}\mathcal{L}_{\rm obs} \tag{2.29}$$

The first, $\mathcal{L}_{\rm GCE}$, is a likelihood calculated using the GCE data in Tables A.1 and A.2 and comparing it to that predicted by the parameters. The second component of the likelihood, $\mathcal{L}_{\rm obs}$, compares the predicted density of resolved MSPs to the observed MSP data.

Before the likelihood can be found it is necessary to find the number of MSPs in the disk and bulge implied by the parameters. Let $p_{\rm d}$ and $p_{\rm b}$ be the probability of an MSP being observed in the disk and bulge respectively, then $N_{\rm disk}$ and $N_{\rm bulge}$ can be found using the following two equations:

$$\begin{aligned} \lambda_{\rm res} &= p_{\rm d}N_{\rm disk} + p_{\rm b}N_{\rm bulge} \\ r_{\rm d/b} &= N_{\rm disk}/N_{\rm bulge} \end{aligned} \tag{2.30}$$

Solving for $N_{\rm disk}$ and $N_{\rm bulge}$ gives:

$$\begin{aligned} N_{\rm disk} &= \frac{\lambda_{\rm res}}{p_{\rm d} + p_{\rm b}/r_{\rm d/b}} \\ N_{\rm bulge} &= \frac{\lambda_{\rm res}}{p_{\rm d}r_{\rm d/b} + p_{\rm b}} \end{aligned} \tag{2.31}$$

It is not practical to find $p_{\rm d}$ and $p_{\rm b}$ exactly as this would require a multidimensional integral for every iteration of the MCMC algorithm. A simplistic way to approximate $p_{\rm d}$ or $p_{\rm b}$ would be to draw a large number of simulated MSPs from the corresponding model (disk or bulge) and use the fraction that are resolved. However, this method has a significant disadvantage, the number of MSPs that it would be necessary to simulate to ensure the result is reasonably accurate could potentially be extremely large. This is because the number of simulated MSPs that are resolved is Poisson distributed, therefore for a relative error of on the order of 1% we may wish to continue drawing from the disk model until we have several thousand resolved (usually $p_{\rm b} \ll p_{\rm d}$ and $r_{\rm d/b} \sim 1$ so accuracy is less important for the bulge), but for luminosity functions which produce few highly luminous MSPs this could mean millions of draws from the model.

There is a simple improvement that can be made by recognising that position in

l, b and d allows a luminosity threshold $L_{\rm th}$ to be found. Before running the MCMC algorithm for each Markov chain, distributions of points were generated according to the disk and bulge spatial models and the position of each point was converted to l, b and d, in addition, for each point, a random number u was drawn from the unit normal distribution to allow us to account for the uncertain flux threshold. Using Eq. (2.15) and the fact that the logarithm of the flux threshold is normally distributed with scale parameter $\sigma_{\rm th}$, the luminosity threshold for point i is:

$$L_{{\rm th},i} = 4\pi d_i^2 \exp(\mu_{\rm th}(l_i, b_i) + K_{\rm th} + \sigma_{\rm th} u_i) \tag{2.32}$$

For any proposed set of parameters the probability of a single random MSP being observed is then:

$$p \approx \frac{1}{N} \sum_{i=1}^{N} p(L > L_{{\rm th},i}) \tag{2.33}$$

where N is the total number of points, $p(L > L_{{\rm th},i})$ is the probability that a randomly generated luminosity is greater than the threshold and p represents either $p_{\rm d}$ or $p_{\rm b}$. Because the same spatial distribution and distribution of u_i is used for each iteration of the algorithm, it can be guaranteed that a particular set of parameters will always give the same result for $N_{\rm disk}$ and $N_{\rm bulge}$. A further improvement that was made involved generating distant points with lower probability but giving them a larger weight in the calculation of p. This ensures a larger proportion of points have relatively low $L_{{\rm th},i}$. Without this, if the luminosity function parameters give a distribution heavily weighted towards lower luminosities, p might effectively depend on a small number of points. Not only could this result in large errors, but if this issue is resolved by simply generating more points, it also means a large amount of time is spent evaluating $p(L > L_{{\rm th},i})$ which have a negligible contribution.

The expected excess that would be produced by the bulge MSPs can be found by multiplying $N_{\rm bulge}$ by the expected contribution of a single MSP. The GCE likelihood is:

$$\mathcal{L}_{\rm GCE} \propto \prod_{i=1}^{N} \exp\left(- \left(\left(\frac{{\rm d}N}{{\rm d}E} \right)_{{\rm sim},i} - \left(\frac{{\rm d}N}{{\rm d}E} \right)_{{\rm data},i} \right)^2 / 2\sigma^2_{{\rm data},i} \right) \tag{2.34}$$

where $\left(\frac{{\rm d}N}{{\rm d}E}\right)_{{\rm sim},i}$ and $\left(\frac{{\rm d}N}{{\rm d}E}\right)_{{\rm data},i}$ are respectively the simulated and observed GCE with uncertainty $\sigma^2_{{\rm data},i}$ at E_i. Before running the MCMC algorithm, a large number of points were generated following the bulge model but without assigning any luminosity. Using the distances and spectral parameters for each point, Eq. (2.20) and

Eq. (2.15), a proportionality constant per unit luminosity for the spectrum can be found allowing $\left(\frac{1}{L}\frac{\mathrm{d}N}{\mathrm{d}E}\right)$ to be calculated for any E. From this result, the expected differential flux per unit luminosity $\langle\frac{1}{L}\frac{\mathrm{d}N}{\mathrm{d}E}\rangle_i$ was estimated for each E_i by taking the mean $\left(\frac{1}{L}\frac{\mathrm{d}N}{\mathrm{d}E}\right)_i$. As they do not contribute, the differential flux for points outside the region of interest was set to 0. The distribution of $\left(\frac{1}{L}\frac{\mathrm{d}N}{\mathrm{d}E}\right)_i$ is independent of the luminosity distribution, so for each iteration of the MCMC algorithm, the expected GCE at E_i is:

$$\begin{aligned}\left(\frac{\mathrm{d}N}{\mathrm{d}E}\right)_{\mathrm{sim},i} &= N_{\mathrm{bulge}}\left\langle\frac{\mathrm{d}N}{\mathrm{d}E}\right\rangle_i \\ &= N_{\mathrm{bulge}}\left\langle L\left(\frac{1}{L}\frac{\mathrm{d}N}{\mathrm{d}E}\right)\right\rangle_i \\ &= N_{\mathrm{bulge}}\langle L\rangle\left\langle\frac{1}{L}\frac{\mathrm{d}N}{\mathrm{d}E}\right\rangle_i\end{aligned} \tag{2.35}$$

where $\langle L\rangle$ is the expectation value of the luminosity function and $\left\langle\frac{\mathrm{d}N}{\mathrm{d}E}\right\rangle_i$ is the expected differential flux for a single MSP.

The second component of the likelihood $\mathcal{L}_{\mathrm{obs}}$, using the form of Eq. 2.28, is proportional to the product of $\exp(-\lambda_{\mathrm{res}})$ and the average density of resolved MSPs at l_i, b_i and d_i weighted according to the observed flux and it's uncertainty:

$$\mathcal{L}_{\mathrm{obs}} \propto \exp(-\lambda_{\mathrm{res}})\prod_{i=1}^{N_{\mathrm{obs}}}\left(\rho_{\mathrm{disk}}(r_{\mathrm{cyl},i}, z_i, N_{\mathrm{disk}}) + \rho_{\mathrm{bulge}}(r_{\mathrm{sph},i}, N_{\mathrm{bulge}})\right) d_i^2 \int_{-\infty}^{\infty} f(\ln(F_i))\,\mathrm{d}\ln(F_i) \tag{2.36}$$

where i represents an observed MSP of which there are N_{obs}. The factor d_i^2 is the Jacobian for the transformation of the MSP density distribution to the spherical coordinate system [33]. The cylindrical and spherical coordinates $r_{\mathrm{cyl},i}$, z_i and $r_{\mathrm{sph},i}$ can be found from l_i, b_i and d_i:

$$\begin{aligned} r_{\mathrm{cyl},i} &= \sqrt{d_i^2 - d_i^2\sin^2(b_i) - 2d_i\cos(b_i)\cos(l_i)r_\odot + r_\odot^2} \\ z_i &= d_i\sin(b_i) \\ r_{\mathrm{sph},i} &= \sqrt{d_i^2 - 2d_i\cos(b_i)\cos(l_i)r_\odot + r_\odot^2}\end{aligned} \tag{2.37}$$

and $f(\ln(F_i))$ is:

$$f(\ln(F_i)) \propto p(F_i > F_{\mathrm{th},i})p(F_i|F_{\mathrm{data},i}, \sigma_{\mathrm{data},i})p(\ln(L_i)) \tag{2.38}$$

where $p(F_i > F_{\mathrm{th},i})$ is the probability the flux is greater than the threshold for galactic coordinates l_i and b_i, $p(\ln(L_i))$ is the log luminosity probability distribution with $L_i = 4\pi d_i^2 F_i$ and $p(F_i|F_{\mathrm{data},i}, \sigma_{\mathrm{data},i})$ is a normal distribution with the observed flux and uncertainty as the mean and standard deviation respectively. In practice, $f(\ln(F_i))$ was only numerically integrated in the region where it was not negligible. This integral is equivalent to an integral over linear flux:

$$\int_{-\infty}^{\infty} f(\ln(F_i))\,\mathrm{d}\ln(F_i) \propto \int_{0}^{\infty} f(F_i)\,\mathrm{d}F_i \tag{2.39}$$

where:

$$\begin{aligned} f(F_i) &\propto p(F_i > F_{\mathrm{th},i}) p(F_i|F_{\mathrm{data},i}, \sigma_{\mathrm{data},i}) p(L_i) 4\pi d_i^2 \\ &= p(F_i > F_{\mathrm{th},i}) p(F_i|F_{\mathrm{data},i}, \sigma_{\mathrm{data},i}) p(L_i) \frac{L_i}{F_i} \\ &= p(F_i > F_{\mathrm{th},i}) p(F_i|F_{\mathrm{data},i}, \sigma_{\mathrm{data},i}) p(\ln(L_i)) \frac{1}{F_i} \end{aligned} \tag{2.40}$$

The $4\pi d_i^2 = \frac{L_i}{F_i}$ is the Jacobian of the transformation from flux to luminosity [33]. The Jacobian for a transformation from x to $\ln(x)$ is x, this allows $p(L_i)L_i$ to be replaced with $p(\ln(L_i))$. This same transformation also means $f(\ln(F_i)) = f(F_i)F_i$, resulting in Eq. (2.38).

Twelve Markov chains were constructed of five million iterations each for four different models. These were the cases where the bulge was spherically symmetric or X-shaped and where the lognormal or simple power law luminosity functions were used.

Chapter 3

Results

For each of the four models corner plots are presented [39] showing the results of the MCMC simulations. These figures show histograms of the two parameters associated with the number of MSPs ($\lambda_{\rm res}$ and $\ln\big(r_{\rm d/b}\big)$), the luminosity function parameters, and the two flux threshold distribution parameters. In addition to those histograms, these figures display the distributions for each pair of model parameters along with 68% and 95% contours. The distance parameters are not shown as these were nuisance parameters necessary to convert from flux to luminosity while, for those without parallax measurements, exploring a wide range of possible distances. In tables, the mean, statistical error, systematic error, and total error are given for each of the parameters where the total errors are the statistical and systematic errors added in quadrature. The units for $L_{\rm med}$, $L_{\rm min}$ and $L_{\rm max}$ are erg s^{-1}. The systematic errors were estimated using four variations of the spatial model. Whereas the main results were produced using $(\sigma_r, \sigma_z) = (5\text{ kpc}, 0.75\text{ kpc})$, the systematic errors used $(4\text{ kpc}, 0.75\text{ kpc})$, $(7\text{ kpc}, 0.75\text{ kpc})$, $(5\text{ kpc}, 0.5\text{ kpc})$ and $(5\text{ kpc}, 1\text{ kpc})$. If μ was the mean from the main spatial model for a particular parameter, the systematic error is:

$$\sigma_{\rm syst} = \sqrt{\frac{1}{4}\sum_{i=1}^{4}(\mu_i - \mu)^2} \tag{3.1}$$

where μ_i are the means for each of the four pairs of spatial parameters.

To show that the distribution of model parameters from the Markov chains fits the observed data well, for each chain the parameters of a few thousand evenly spaced points were used to generate a simulated set of resolved MSPs. This simulated data was binned in l, b, $\log_{10}(F)$ and $\log_{10}(d)$ and the means and standard deviations of each bin are compared to the observed data in a set of figures for each model. The distribution of the simulated GCE is also plotted along with the measured data. A

pair of plots are also shown which display the distribution of the number of simulated resolved MSPs both inside and outside the projected bulge region compared with the observations. The projected bulge region is all galactic coordinates where the probability of a bulge MSP being modeled is non-zero. It can be seen for each bulge model in Figs. 2.2 and 2.3.

For every step in the Markov chains, the expected number of observed bulge MSPs was found along with the expected number for the cases where the flux thresholds were divided by factors of two and four. Using the series of expected values for each of the three cases, Poisson distributions were randomly sampled giving a discrete distribution of values N, the number of resolved bulge MSPs. From these three distributions, the overall probability for getting any N can be estimated. Histograms of these probability distributions are shown for each model along with a table showing the mean and the probability of $N > 0$.

3.1 Lognormal Luminosity Distribution with Spherically Symmetric Bulge

In this section the results for the lognormal luminosity function and spherically symmetric bulge model are presented. In Fig. 3.1, the distribution of points in the set of Markov chains produced for this model is shown. Correlations can be seen between $\log_{10}(L_{\rm med})$ and σ_L as well as between the three parameters $\ln\left(r_{\rm d/b}\right)$, $K_{\rm th}$ and $\sigma_{\rm th}$. Table 3.1 presents the mean and statistical error for each model parameter along with systematic errors associated with uncertainty in the spatial model.

Parameter	Mean	Statistical Error	Systematic Error	Total Error
$\lambda_{\rm res}$	72	9	0.2	9
$\ln\left(r_{\rm d/b}\right)$	0.2	0.3	0.1	0.4
$\log_{10}(L_{\rm med})$	31.9	0.5	0.1	0.5
σ_L	1.4	0.3	0.04	0.3
$K_{\rm th}$	2.3	0.3	0.07	0.3
$\sigma_{\rm th}$	0.7	0.1	0.03	0.1

Table 3.1: Mean values and statistical, systematic and total errors for lognormal luminosity distribution and spherical bulge model parameters.

A set of figures show the results of using the sets of parameters in the Markov chains constructed using this model to simulate populations of MSPs. In Figs. 3.2,

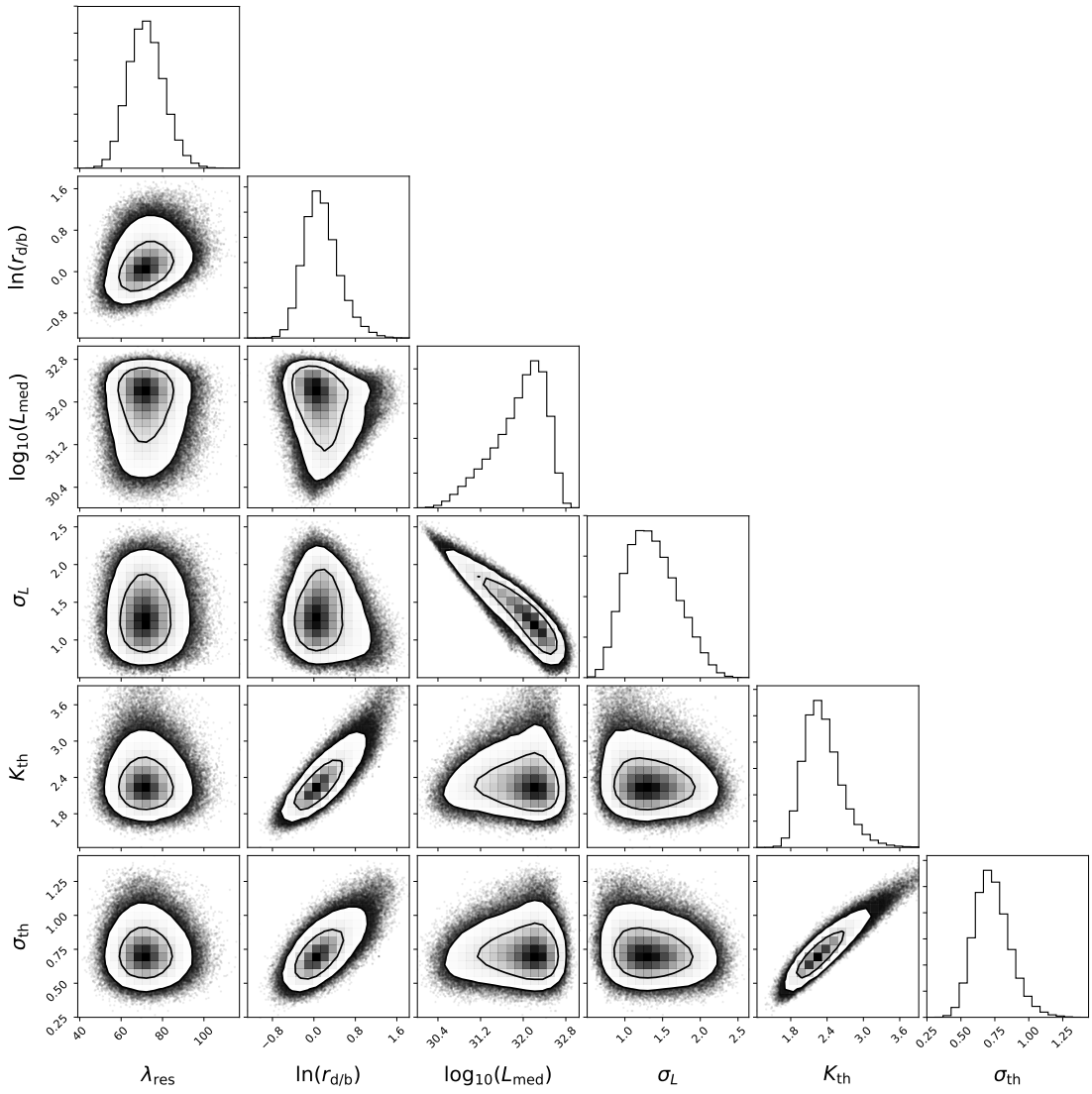

Figure 3.1: Distribution of points in Markov chains for the lognormal luminosity distribution and spherical bulge model.

3.3, 3.4 and 3.5, the binned distributions of resolved MSPs in longitude, latitude, distance and flux are shown. The distribution of the number of resolved MSPs inside and outside of the projected bulge region is seen in 3.6. Fig. 3.7 shows the simulated GCE produced by the bulge population.

Table 3.2 shows the probability of observing any MSPs from the bulge population and the expected number based on the fitted flux threshold parameters as well as where the detection sensitivity has been doubled and quadrupled. These three probability distributions in the number of resolved bulge MSPs are shown in Figs. 3.8 and 3.9.

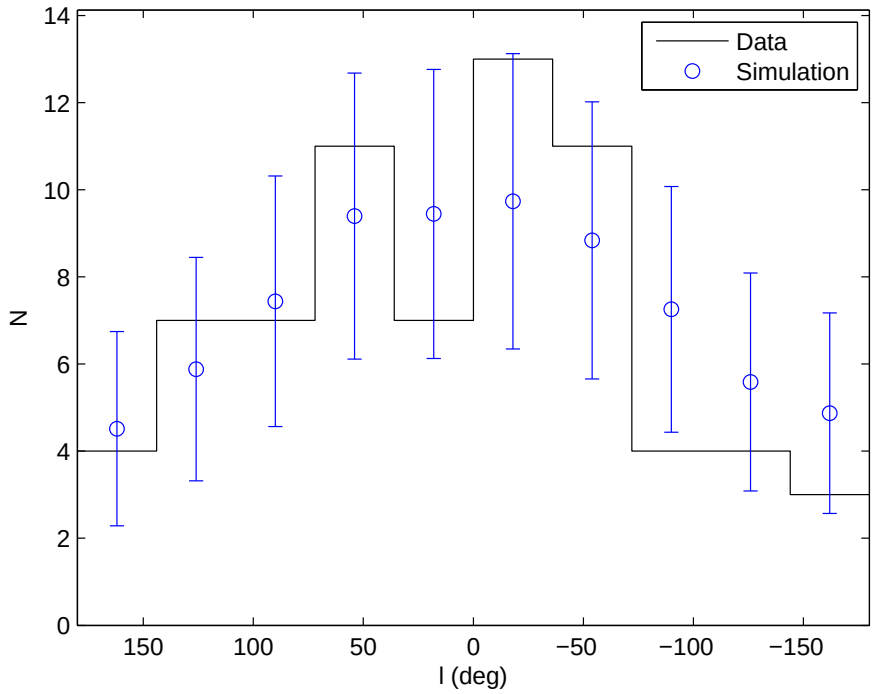

Figure 3.2: Simulated observed distribution of MSPs in longitude for the lognormal luminosity distribution and spherical bulge model.

Sensitivity Factor	Mean N	P($N > 0$)
1.0	0.432	0.262
2.0	2.34	0.636
4.0	11.7	0.913

Table 3.2: Expected number of observed MSPs located in the bulge and probability of observing one or more for lognormal luminosity distribution and spherical bulge model.

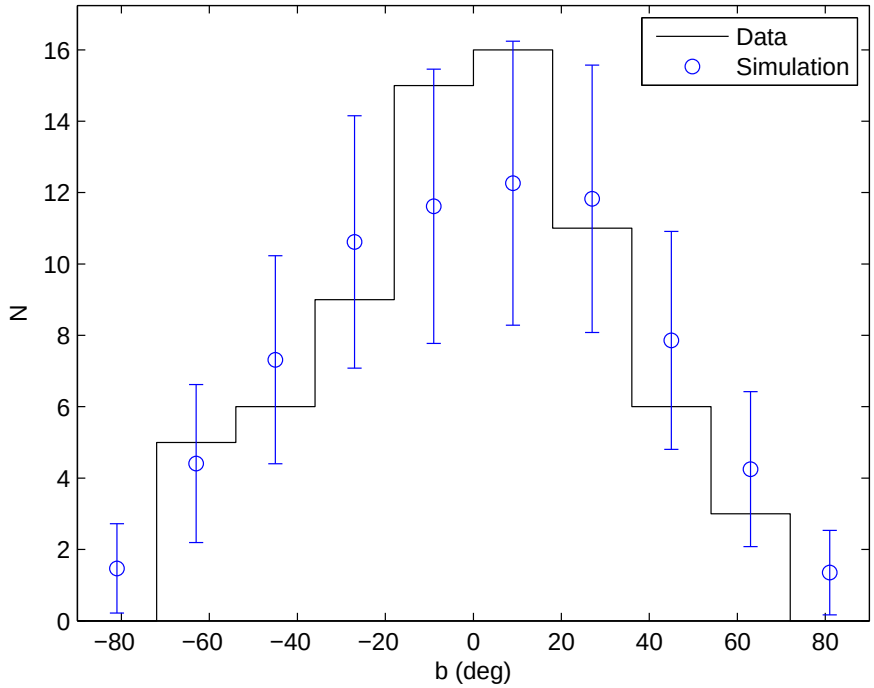

Figure 3.3: Simulated observed distribution of MSPs in latitude for the lognormal luminosity distribution and spherical bulge model.

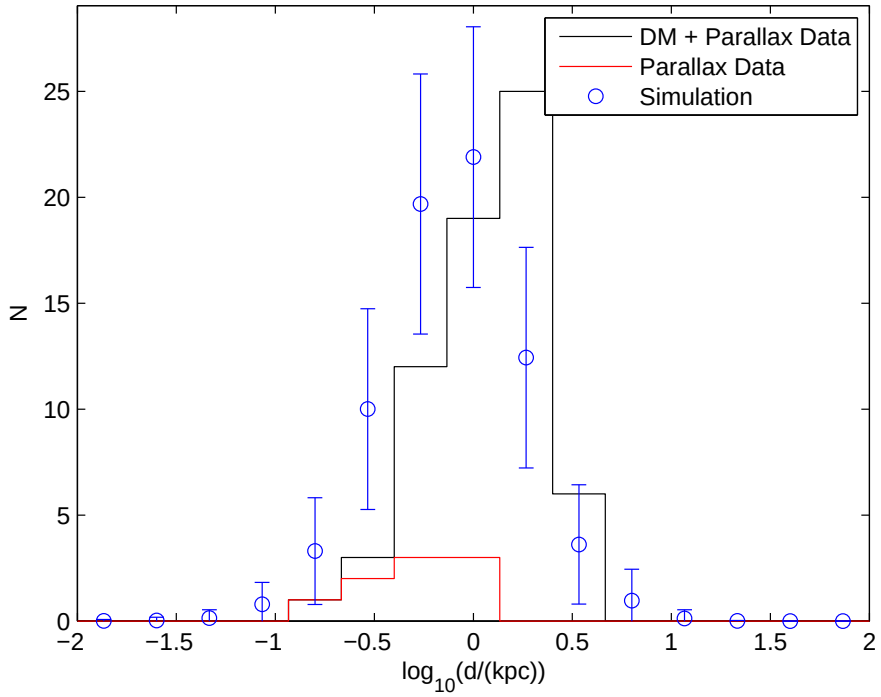

Figure 3.4: Simulated observed distribution of MSPs in distance for the lognormal luminosity distribution and spherical bulge model. DM means dispersion measure derived distances.

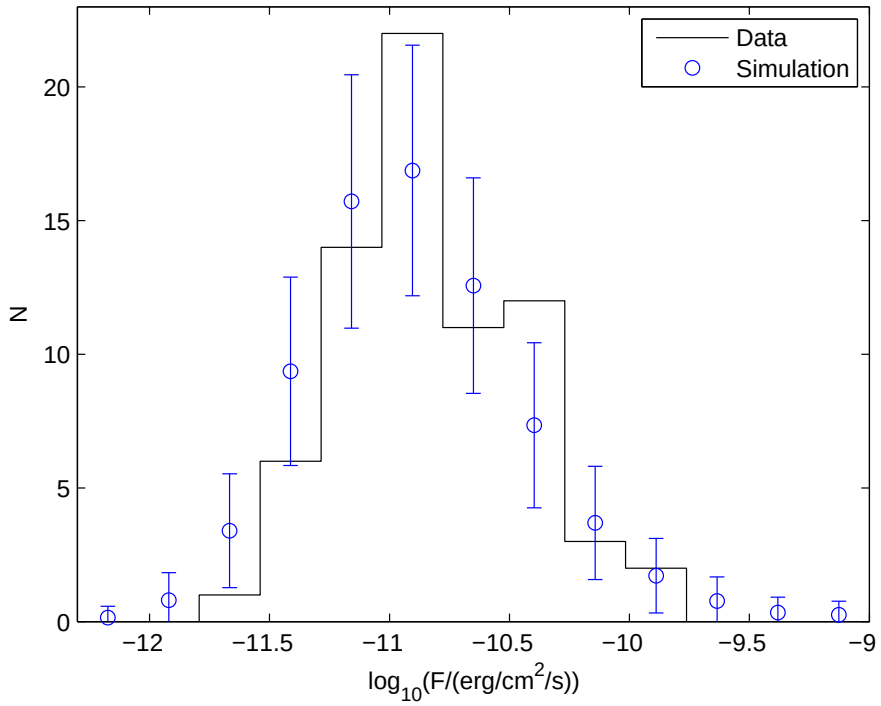

Figure 3.5: Simulated observed distribution of MSPs in flux for the lognormal luminosity distribution and spherical bulge model.

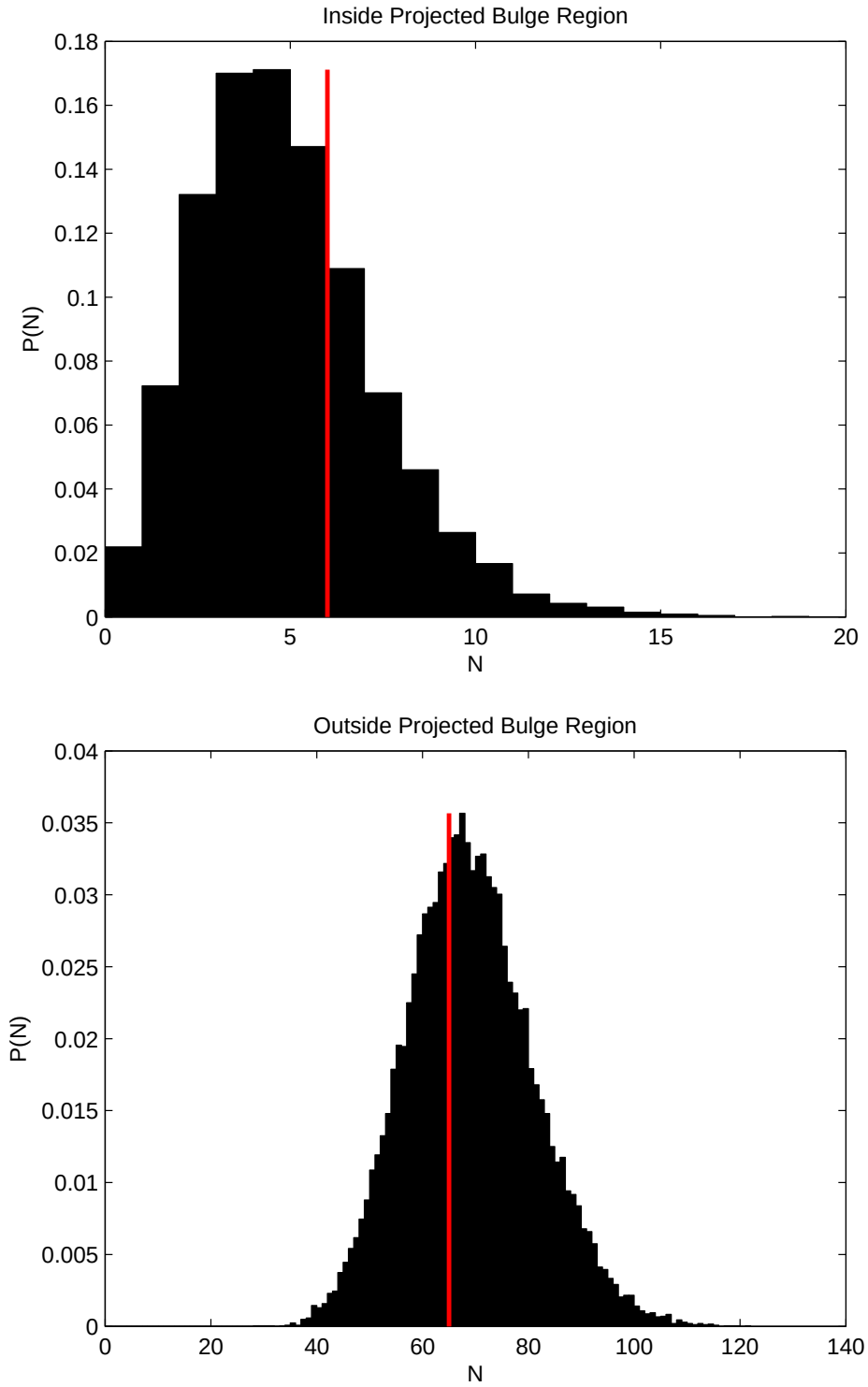

Figure 3.6: The approximate probability distributions of observing N MSPs inside and outside the projected bulge using the lognormal luminosity distribution and spherical bulge model. The red lines are the observed number for each case.

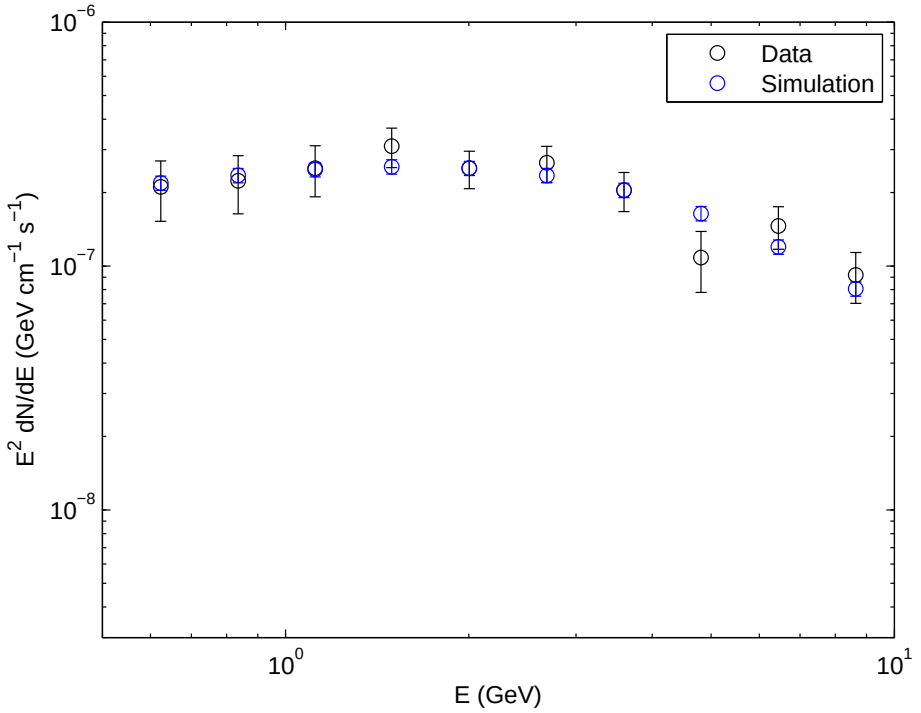

Figure 3.7: Simulated Galactic Center excess for the lognormal luminosity distribution and spherical bulge model.

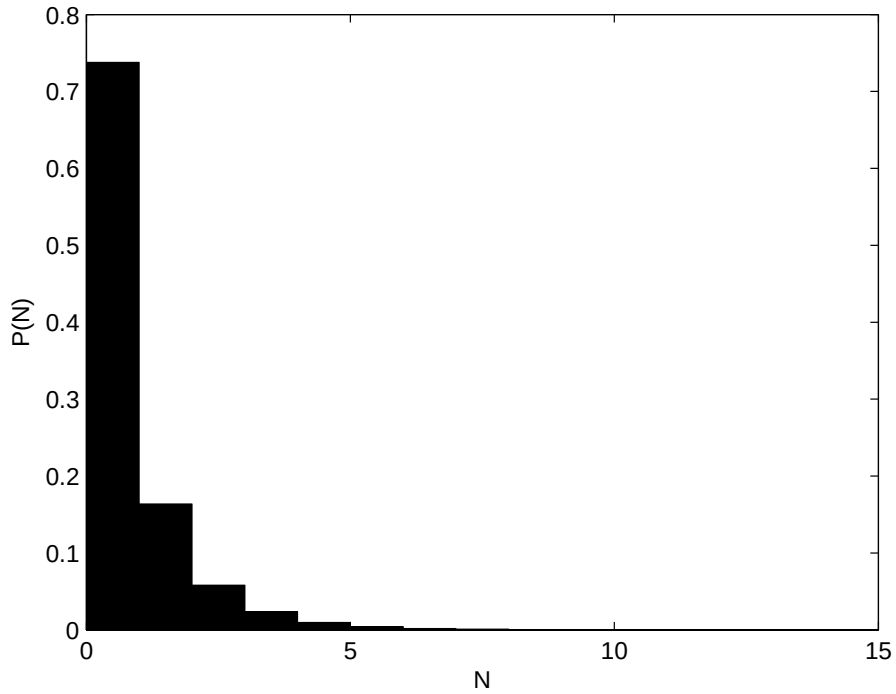

Figure 3.8: The probability distribution of observing N MSPs from the bulge population based on the lognormal luminosity distribution and spherical bulge model.

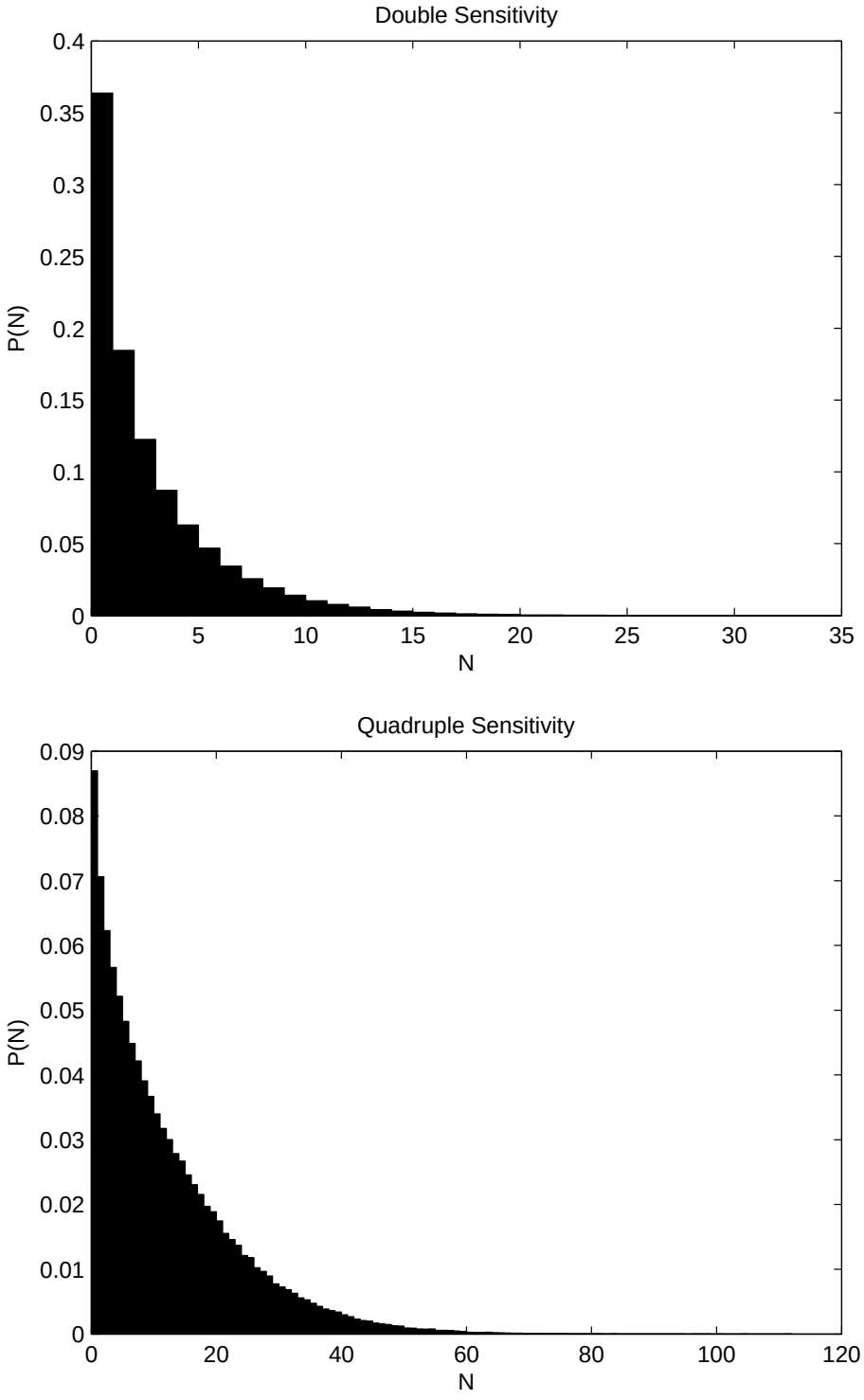

Figure 3.9: The probability distribution of observing N MSPs from the bulge population based on the lognormal luminosity distribution and spherical bulge model with double or quadruple sensitivity.

3.2 Lognormal Luminosity Distribution with X-shaped Bulge

This section presents the results for the model where luminosities have a lognormal distribution and the X-shaped bulge model is used. The MCMC simulation results are shown in 3.10. There are, as for the spherically symmetric bulge case, clear correlations between $\log_{10}(L_{\rm med})$ and σ_L and between the three parameters $\ln\big(r_{\rm d/b}\big)$, $K_{\rm th}$ and $\sigma_{\rm th}$. Means and errors for each of the model parameters are listed in Table 3.3.

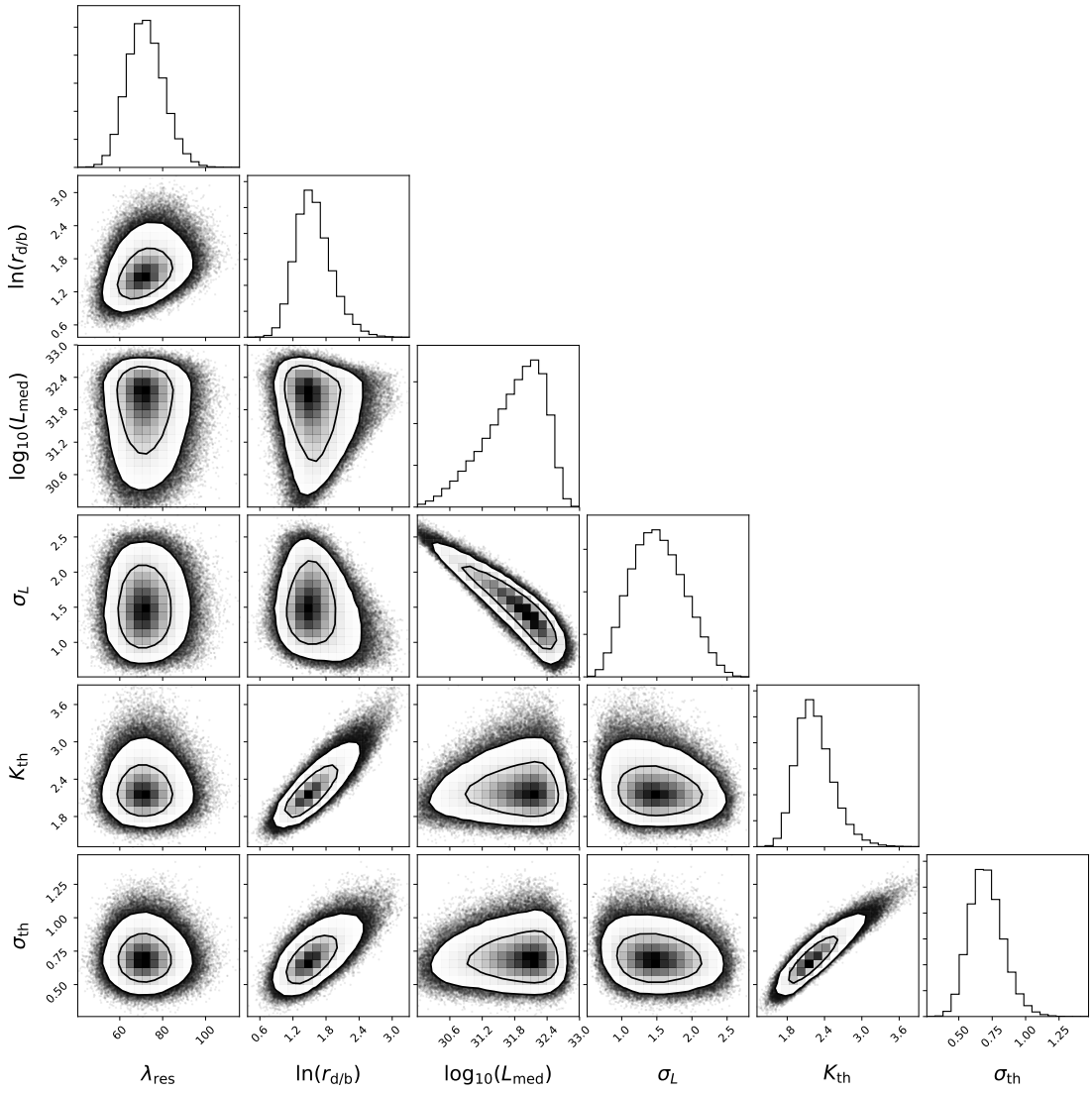

Figure 3.10: Distribution of points in Markov chains for the lognormal luminosity distribution and X-shaped bulge model.

The simulated distributions of resolved MSPs in longitude, latitude, distance

Parameter	Mean	Statistical Error	Systematic Error	Total Error
$\lambda_{\rm res}$	72	8	0.2	8
$\ln\left(r_{\rm d/b}\right)$	1.6	0.3	0.2	0.4
$\log_{10}(L_{\rm med})$	31.8	0.5	0.09	0.6
σ_L	1.5	0.4	0.1	0.4
$K_{\rm th}$	2.2	0.3	0.05	0.3
$\sigma_{\rm th}$	0.7	0.1	0.02	0.1

Table 3.3: Mean values and statistical, systematic and total errors for lognormal luminosity distribution and X-shaped bulge model parameters.

and flux are shown in Figs. 3.11, 3.12, 3.13 and 3.14 with the distribution of the numbers located inside and outside the region of the projected bulge displayed in Fig. 3.15. The GCE that would be caused by the bulge MSPs in plotted in Fig. 3.16.

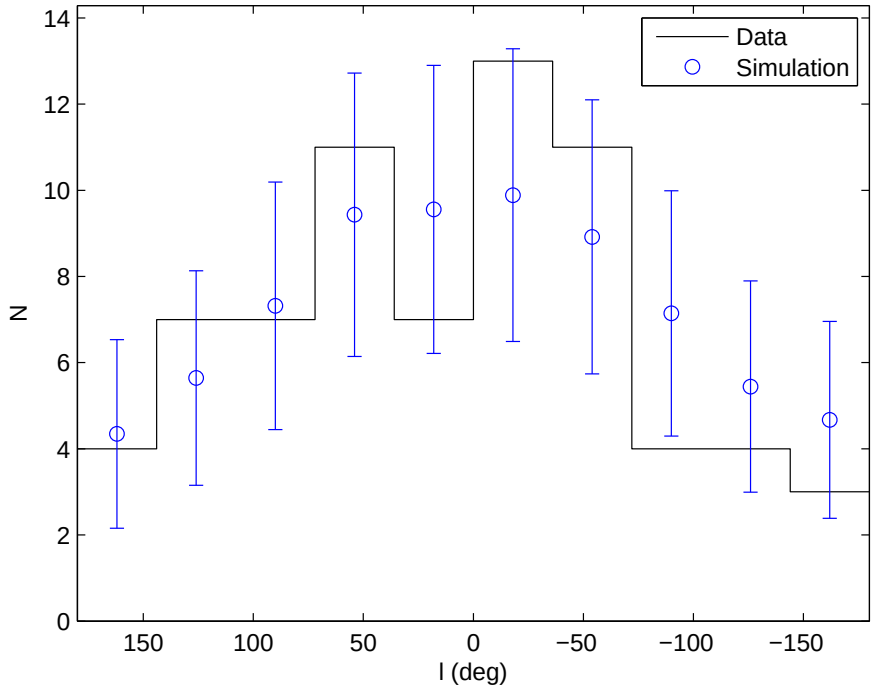

Figure 3.11: Simulated observed distribution of MSPs in longitude for the lognormal luminosity distribution and X-shaped bulge model.

The probabilities of observing one or more bulge MSPs and the expected number of observations are listed in Table 3.4 with the probability distribution of observing N bulge MSPs displayed in Figs. 3.17 and 3.18.

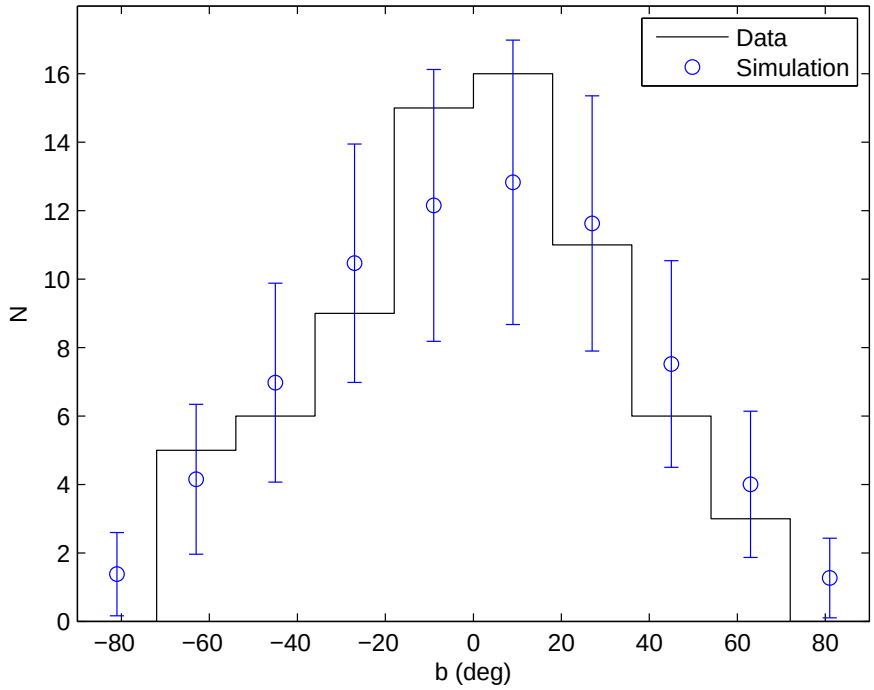

Figure 3.12: Simulated observed distribution of MSPs in latitude for the lognormal luminosity distribution and X-shaped bulge model.

Sensitivity Factor	Mean N	P($N > 0$)
1.0	0.195	0.151
2.0	0.887	0.437
4.0	3.767	0.782

Table 3.4: Expected number of observed MSPs located in the bulge and probability of observing one or more for lognormal luminosity distribution and X-shaped bulge model.

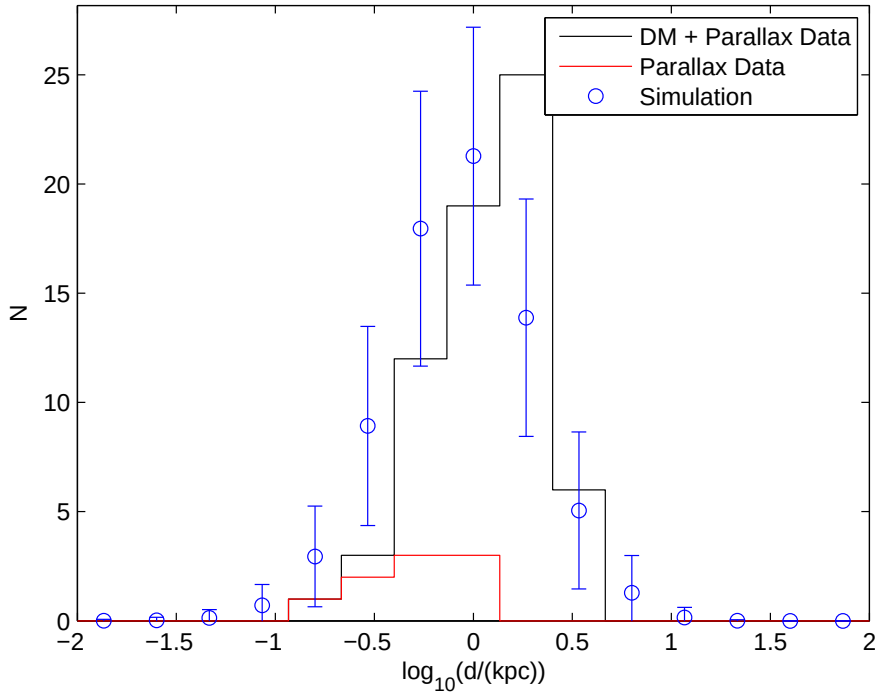

Figure 3.13: Simulated observed distribution of MSPs in distance for the lognormal luminosity distribution and X-shaped bulge model. DM means dispersion measure derived distances.

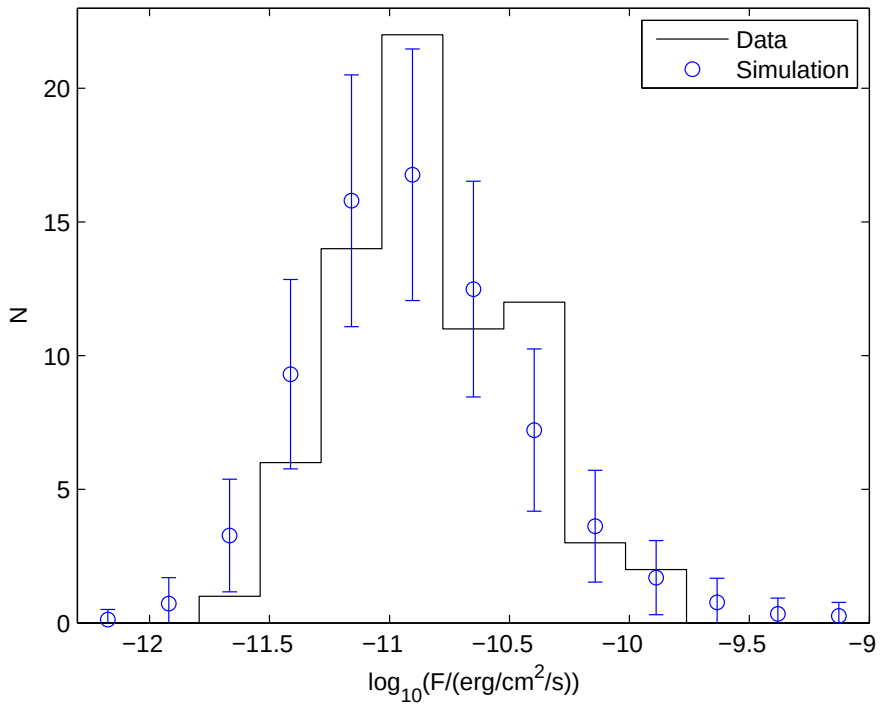

Figure 3.14: Simulated observed distribution of MSPs in flux for the lognormal luminosity distribution and X-shaped bulge model.

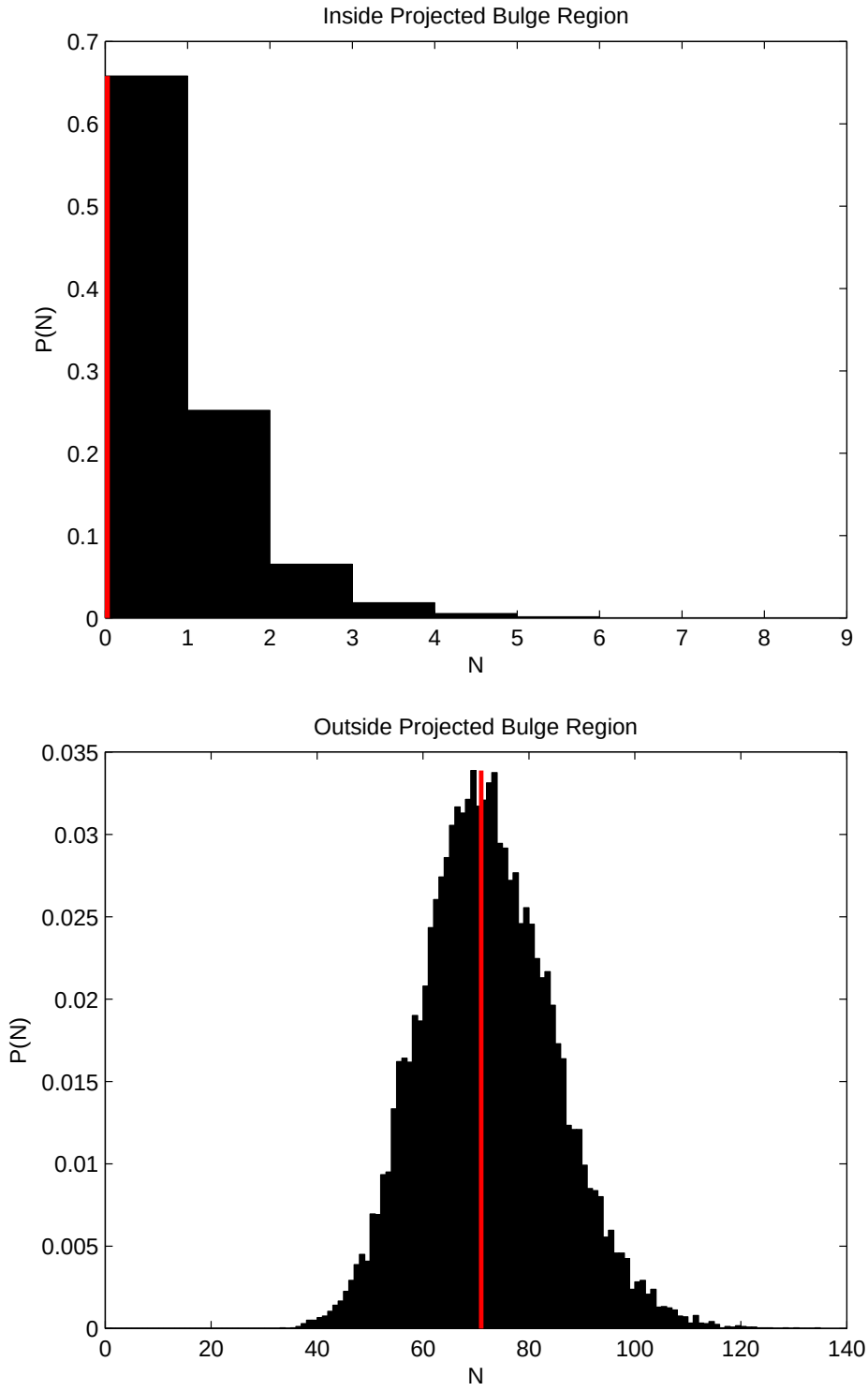

Figure 3.15: The approximate probability distributions of observing N MSPs inside and outside the projected bulge using the lognormal luminosity distribution and X-shaped bulge model. The red lines are the observed number for each case.

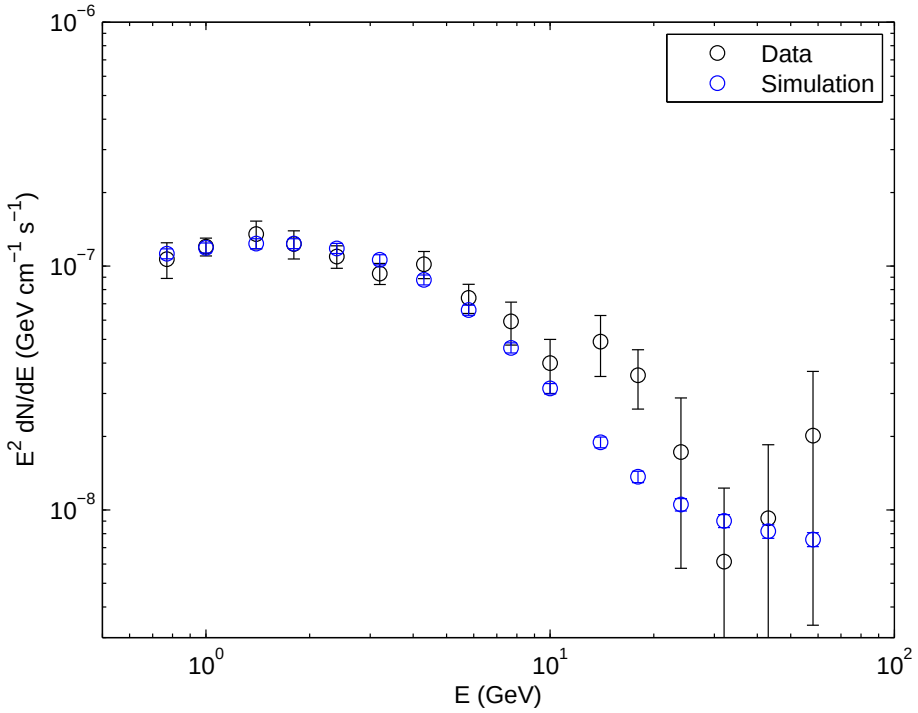

Figure 3.16: Simulated Galactic Center excess for the lognormal luminosity distribution and X-shaped bulge model.

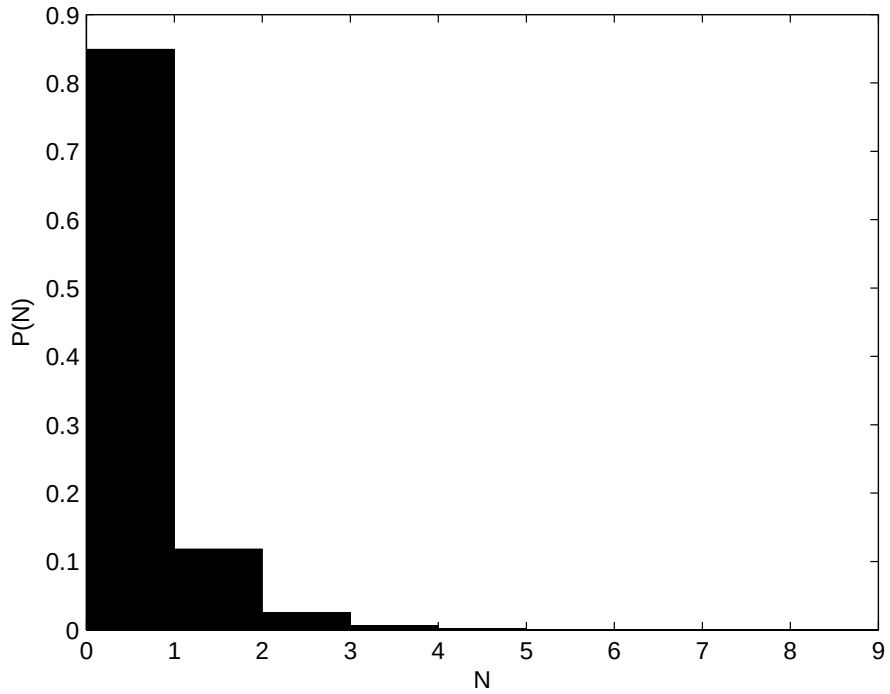

Figure 3.17: The probability distribution of observing N MSPs from the bulge population based on the lognormal luminosity distribution and X-shaped bulge model.

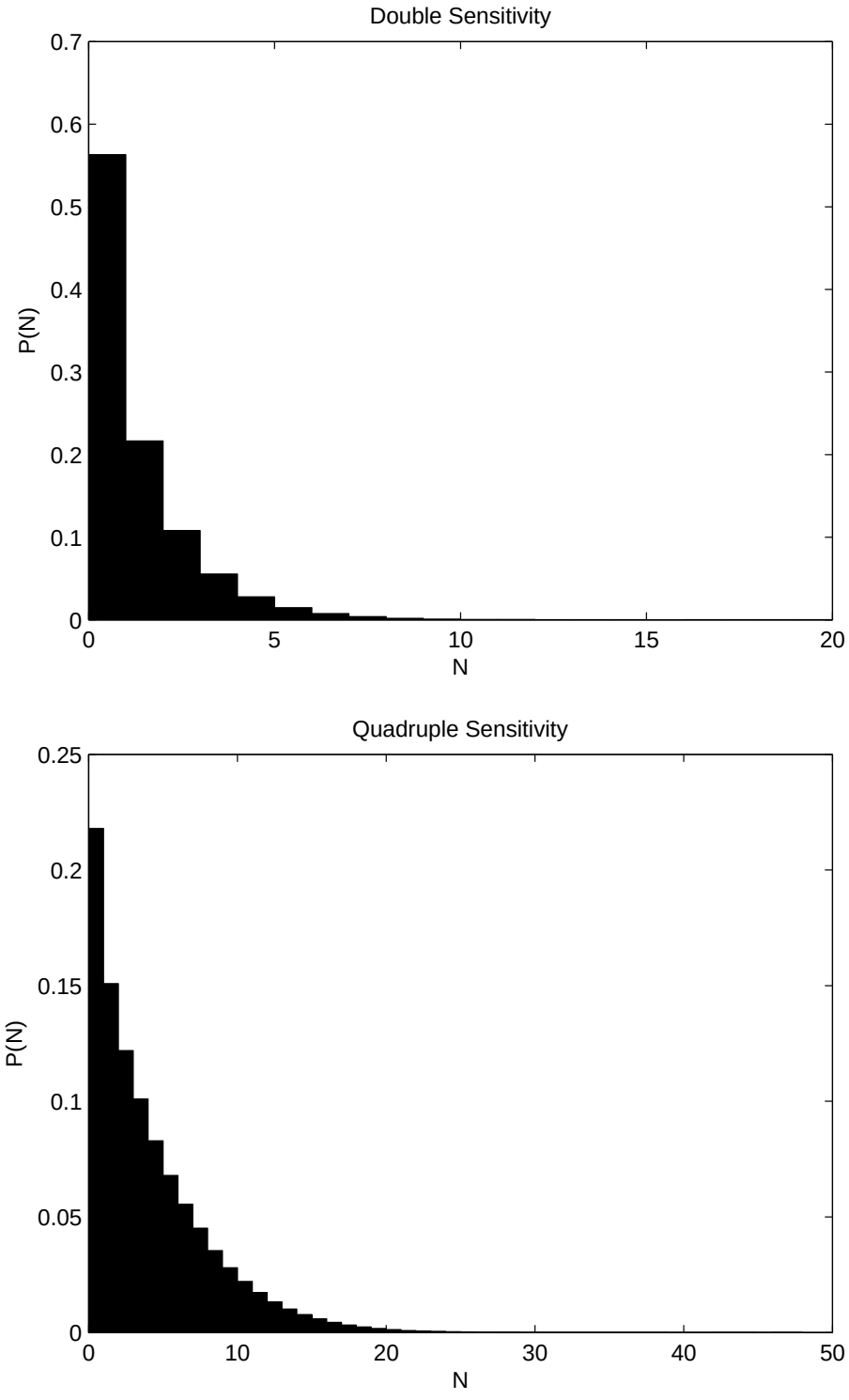

Figure 3.18: The probability distribution of observing N MSPs from the bulge population based on the lognormal luminosity distribution and X-shaped bulge model with double or quadruple sensitivity.

3.3 Simple Power Law Luminosity Distribution with Spherically Symmetric Bulge

The distribution of samples in the Markov chains for the simple power law luminosity function and spherically symmetric bulge model is shown in Fig. 3.19. Again, there is a correlation between the three parameters $\ln\left(r_{\mathrm{d/b}}\right)$, K_{th} and σ_{th}. There is also a banana-shaped relationship visible between α and $\log_{10}(L_{max})$. Table 3.5 lists the means and errors for each of the model parameters.

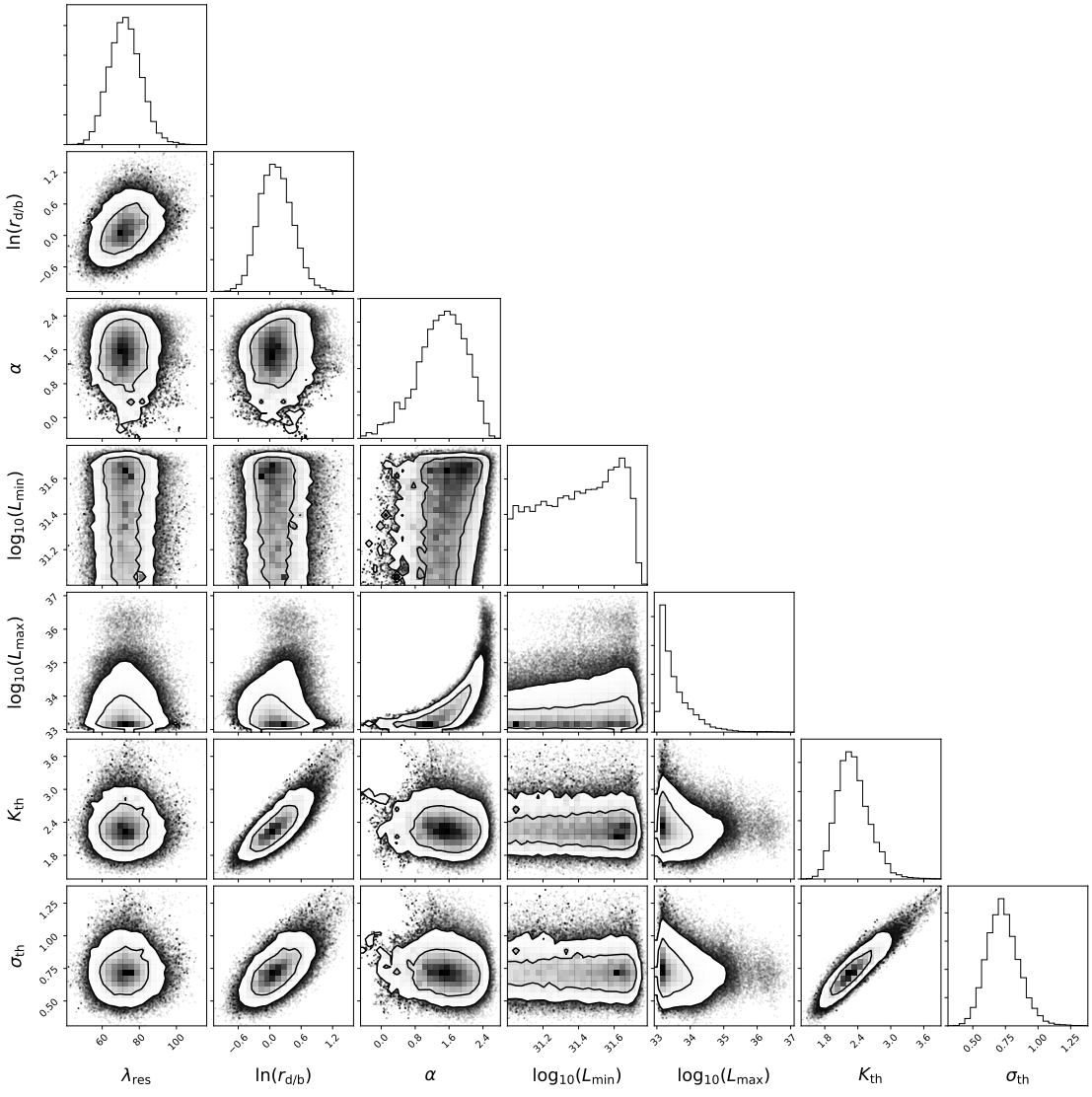

Figure 3.19: Distribution of points in Markov chains for the simple power law luminosity distribution and spherical bulge model.

Figs. 3.20, 3.21, 3.22 and 3.23 show the results of simulating populations of MSPs based on the parameters in the Markov chains. The distributions of the number of

Parameter	Mean	Statistical Error	Systematic Error	Total Error
$\lambda_{\rm res}$	72	8	0.9	9
$\ln(r_{\rm d/b})$	0.1	0.3	0.2	0.4
α	1.4	0.6	0.2	0.6
$\log_{10}(L_{\rm min})$	31.4	0.2	0.01	0.2
$\log_{10}(L_{\rm max})$	33.6	0.5	0.1	0.5
$K_{\rm th}$	2.3	0.3	0.1	0.3
$\sigma_{\rm th}$	0.7	0.1	0.04	0.1

Table 3.5: Mean values and statistical, systematic and total errors for simple power law luminosity distribution and spherical bulge model parameters.

MSPs inside and outside the projected bulge region of the sky are shown in Fig. 3.24. The simulated GCE is displayed in Fig. 3.25.

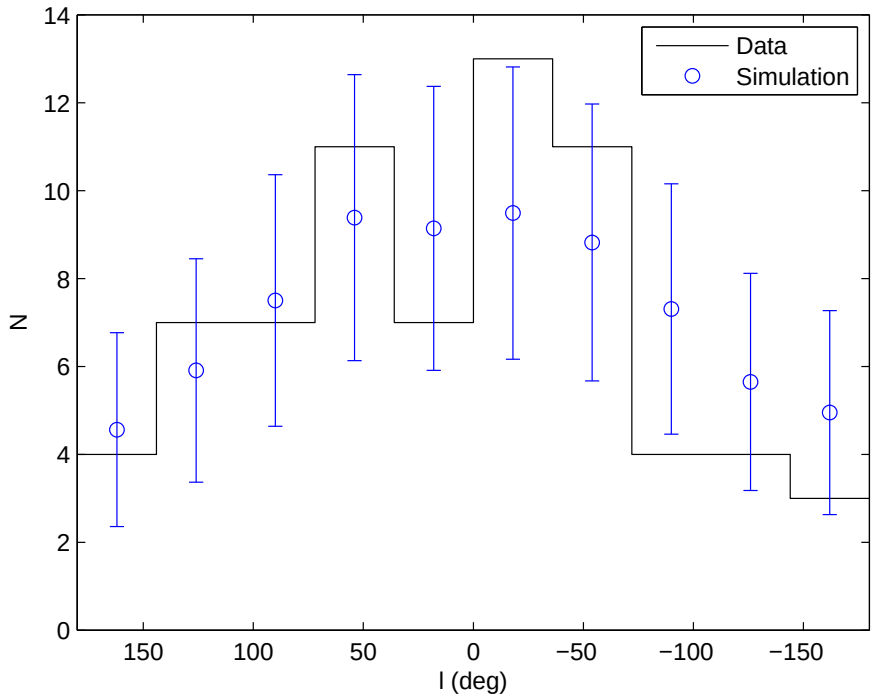

Figure 3.20: Simulated observed distribution of MSPs in longitude for the simple power law luminosity distribution and spherical bulge model.

Table 3.6 lists the probabilities of observing one or more bulge MSPs and the expected number for the fitted flux threshold distribution and the cases where this sensitivity is doubled and quadrupled. The probability of observing N bulge MSPs

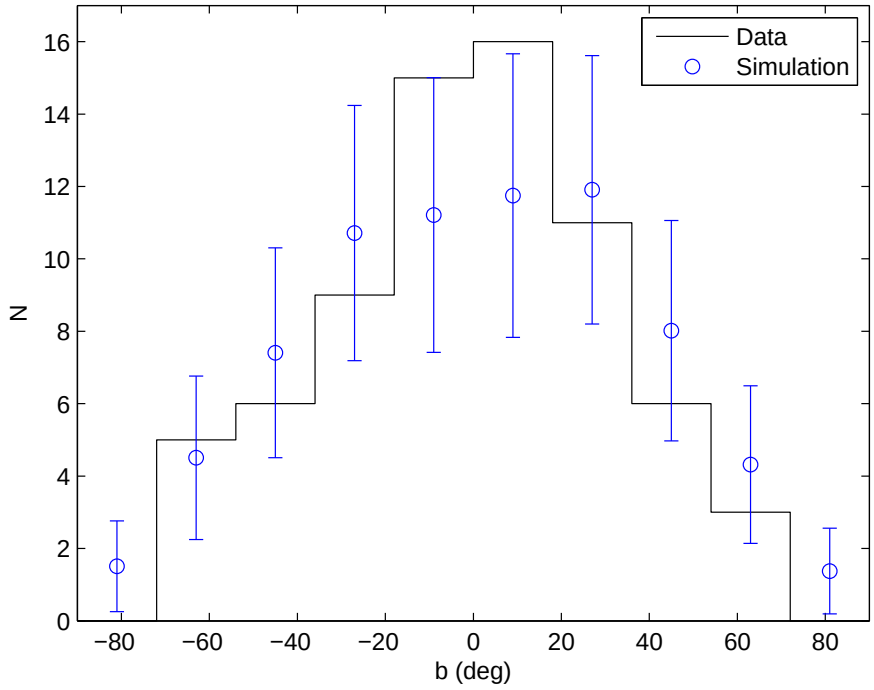

Figure 3.21: Simulated observed distribution of MSPs in latitude for the simple power law luminosity distribution and spherical bulge model.

in the bulge population for each of these three cases is shown in Figs. 3.26 and 3.27.

Sensitivity Factor	Mean N	P($N > 0$)
1.0	0.144	0.0759
2.0	0.990	0.252
4.0	6.46	0.619

Table 3.6: Expected number of observed MSPs located in the bulge and probability of observing one or more for simple power law luminosity distribution and spherical bulge model.

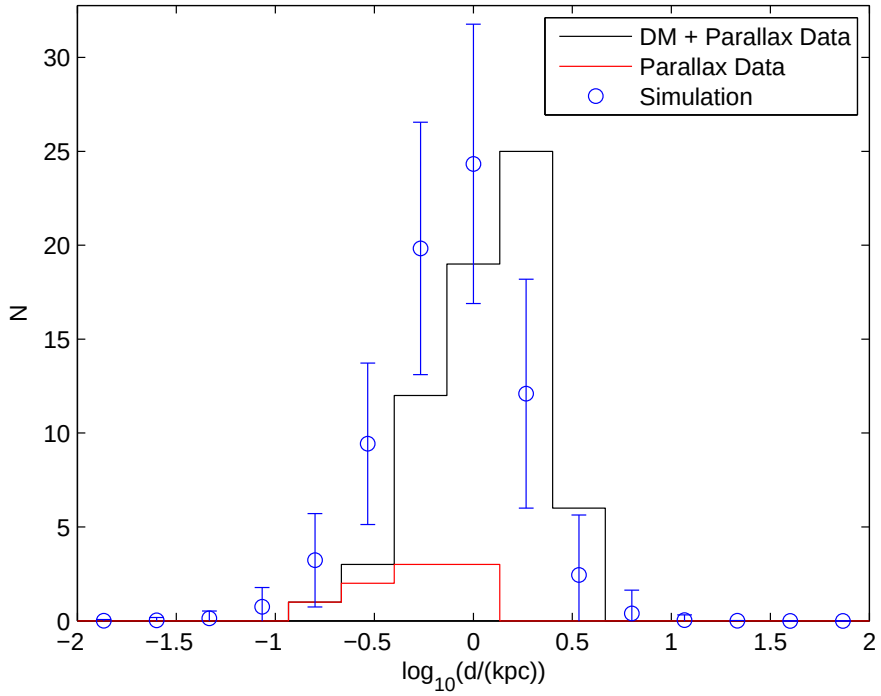

Figure 3.22: Simulated observed distribution of MSPs in distance for the simple power law luminosity distribution and spherical bulge model. DM means dispersion measure derived distances.

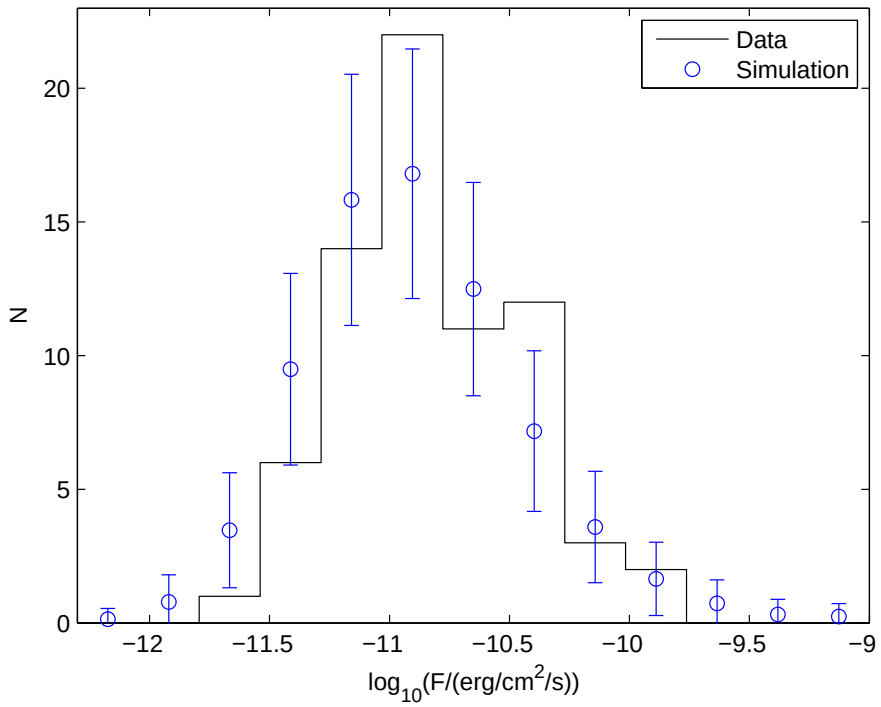

Figure 3.23: Simulated observed distribution of MSPs in flux for the simple power law luminosity distribution and spherical bulge model.

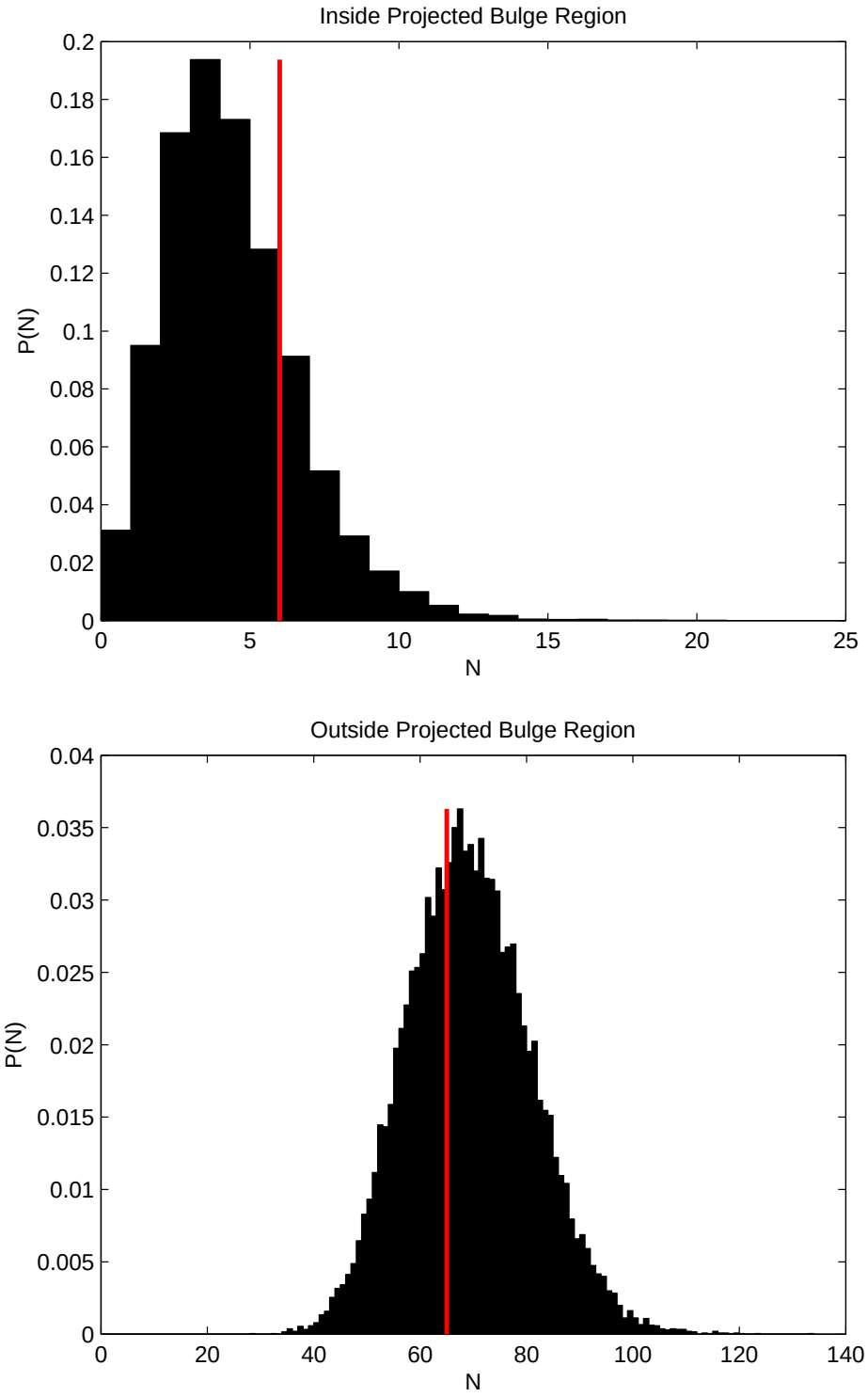

Figure 3.24: The approximate probability distributions of observing N MSPs inside and outside the projected bulge using the simple power law luminosity distribution and spherical bulge model. The red lines are the observed number for each case.

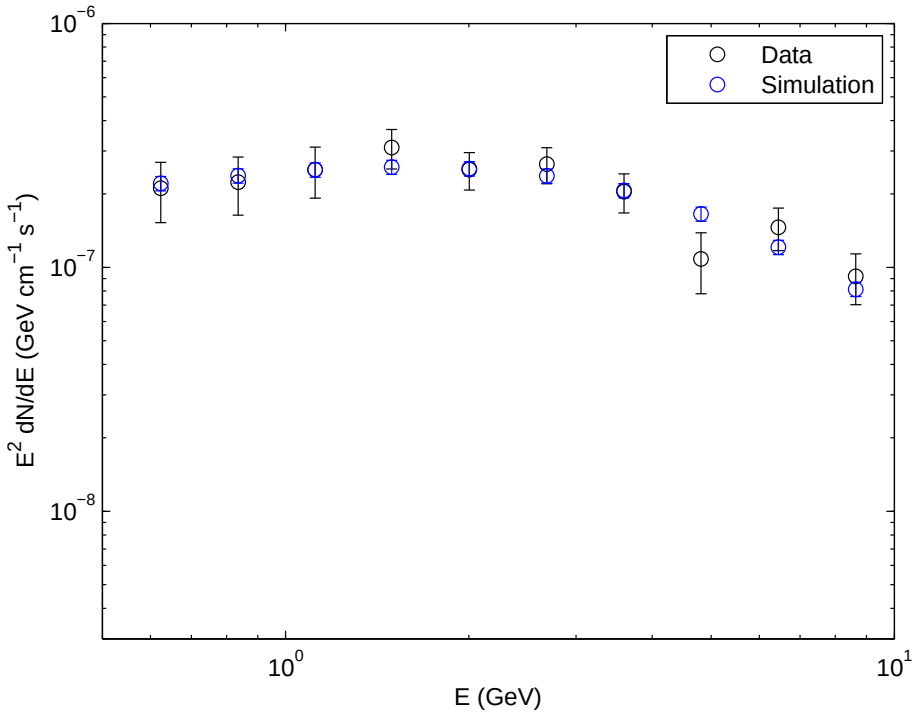

Figure 3.25: Simulated Galactic Center excess for the simple power law luminosity distribution and spherical bulge model.

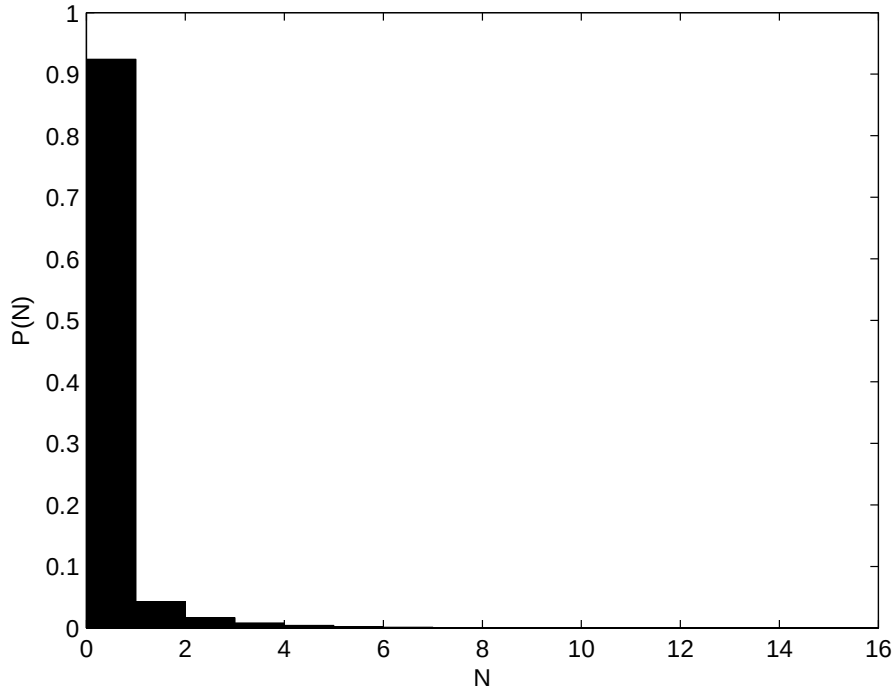

Figure 3.26: The probability distribution of observing N MSPs from the bulge population based on the simple power law luminosity distribution and spherical bulge model.

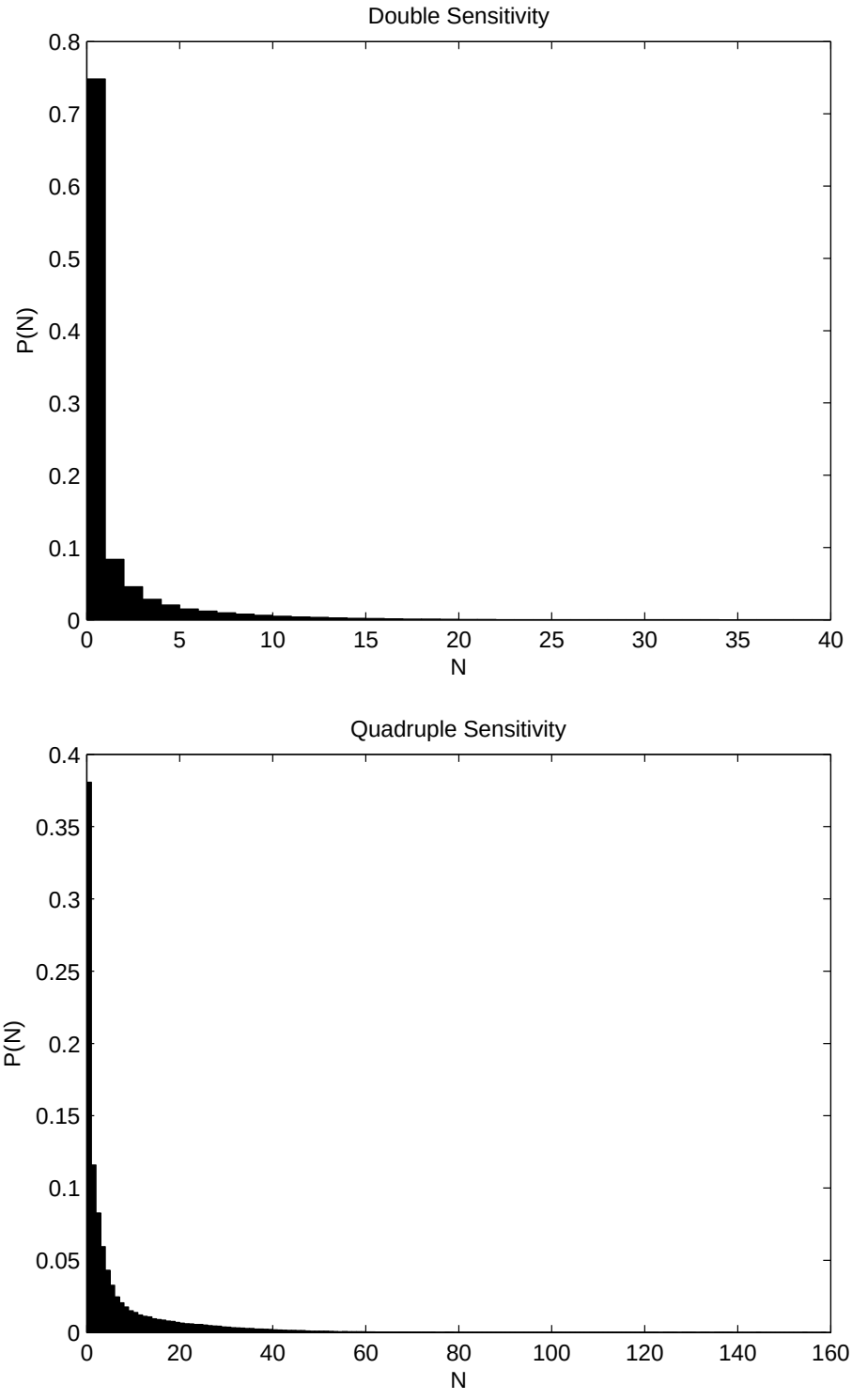

Figure 3.27: The probability distribution of observing N MSPs from the bulge population based on the simple power law luminosity distribution and spherical bulge model with double or quadruple sensitivity.

3.4 Simple Power Law Luminosity Distribution with X-shaped Bulge

The results of the MCMC simulation for the simple power law luminosity distribution with X-shaped bulge model are shown in Fig. 3.28. As with the spherically symmetric bulge model, the banana shaped relationship between α and $\log_{10}(L_{max})$ is seen as well as the correlation between the parameters $\ln\left(r_{\mathrm{d/b}}\right)$, K_{th} and σ_{th}. For each of the model parameters means and errors are given in Table 3.7.

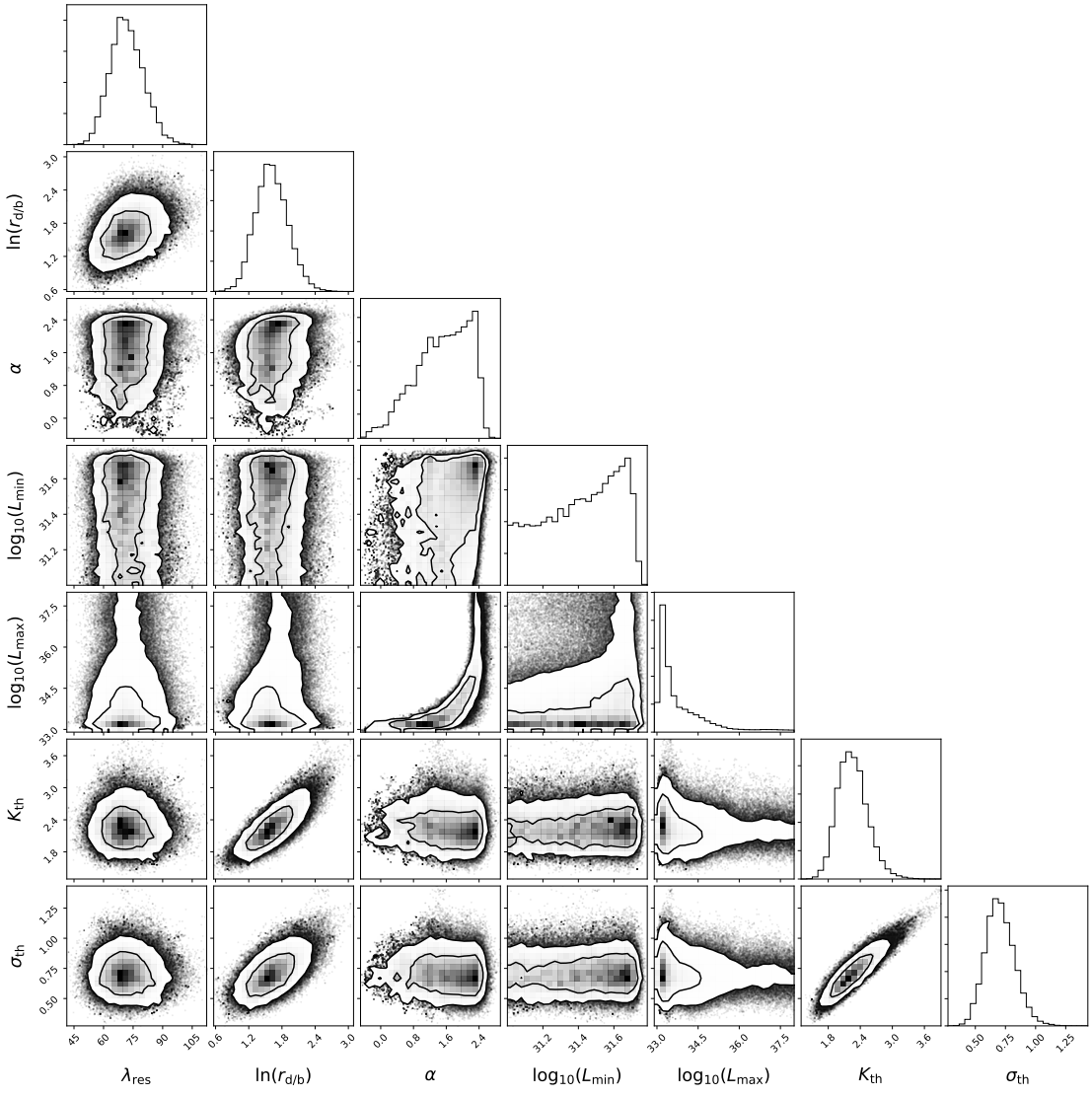

Figure 3.28: Distribution of points in Markov chains for the simple power law luminosity distribution and X-shaped bulge model.

Modelled populations of MSPs using the MCMC results gave the distributions of resolved MSPs shown in Figs. 3.29, 3.30, 3.31 and 3.32. Histograms of the number of

Parameter	Mean	Statistical Error	Systematic Error	Total Error
$\lambda_{\rm res}$	72	8	0.9	9
$\ln(r_{\rm d/b})$	1.6	0.3	0.2	0.4
α	1.5	0.6	0.4	0.8
$\log_{10}(L_{\rm min})$	31.4	0.2	0.05	0.2
$\log_{10}(L_{\rm max})$	34	1	0.5	1
$K_{\rm th}$	2.3	0.3	0.03	0.3
$\sigma_{\rm th}$	0.7	0.1	0.01	0.1

Table 3.7: Mean values and statistical, systematic and total errors for simple power law luminosity distribution and X-shaped bulge model parameters.

simulated MSPs resolved both inside and outside the region of the projected bulge are displayed in Fig. 3.33. The simulated GCE data is plotted in Fig. 3.34.

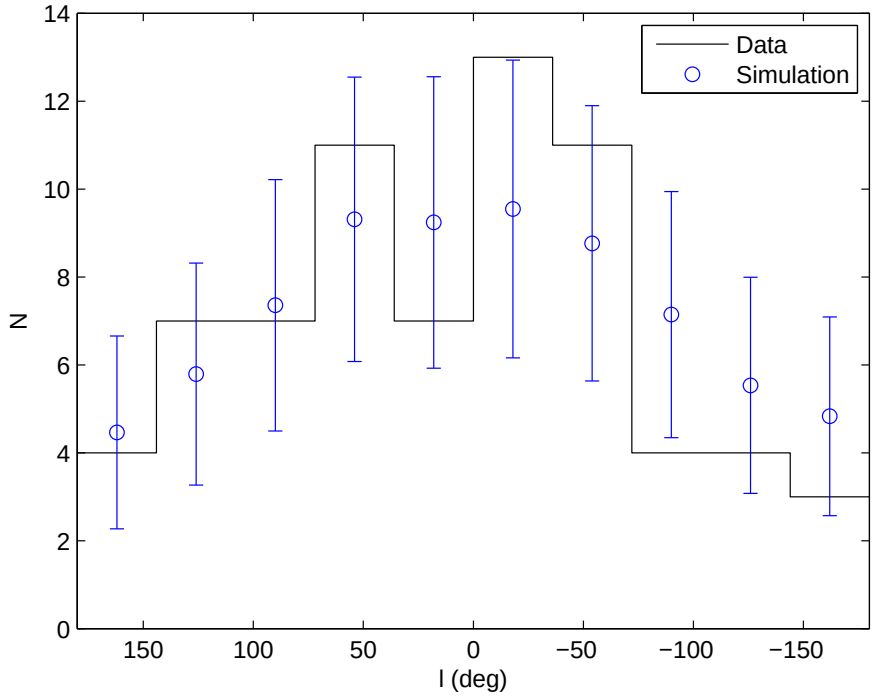

Figure 3.29: Simulated observed distribution of MSPs in longitude for the simple power law luminosity distribution and X-shaped bulge model.

A list of the expected number and probability of one or more observed bulge MSPs is found in Table 3.8 and probability distributions for observing N can be seen in Figs. 3.35 and 3.36.

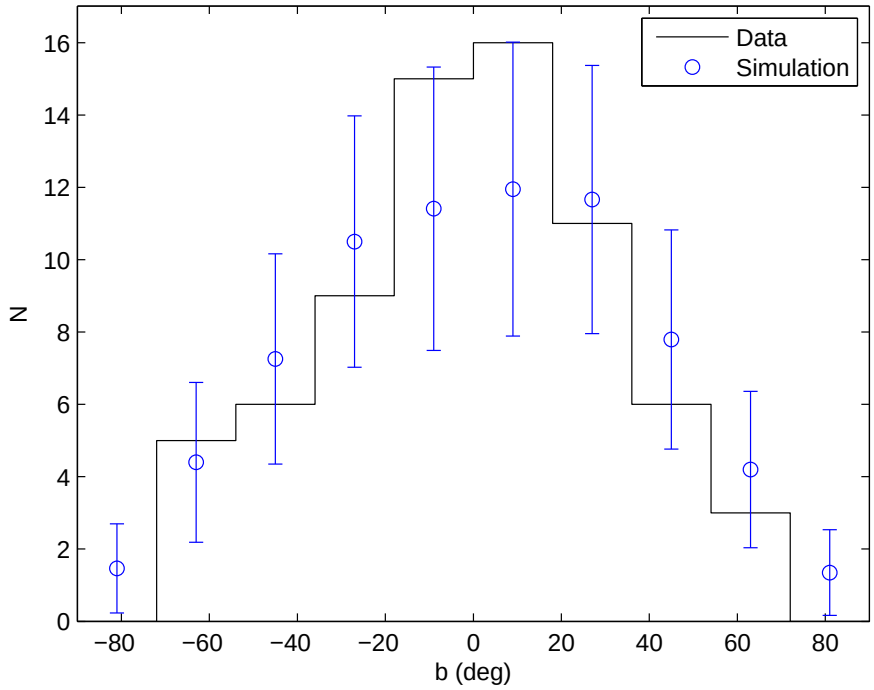

Figure 3.30: Simulated observed distribution of MSPs in latitude for the simple power law luminosity distribution and X-shaped bulge model.

Sensitivity Factor	Mean N	P($N > 0$)
1.0	0.131	0.0870
2.0	0.514	0.208
4.0	2.05	0.368

Table 3.8: Expected number of observed MSPs located in the bulge and probability of observing one or more for simple power law luminosity distribution and X-shaped bulge model.

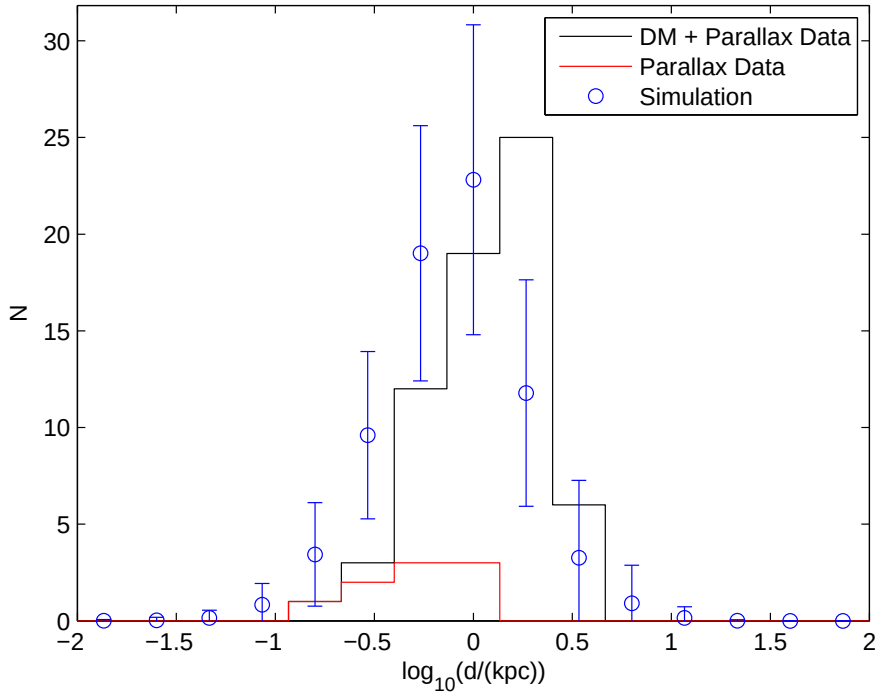

Figure 3.31: Simulated observed distribution of MSPs in distance for the simple power law luminosity distribution and X-shaped bulge model. DM means dispersion measure derived distances.

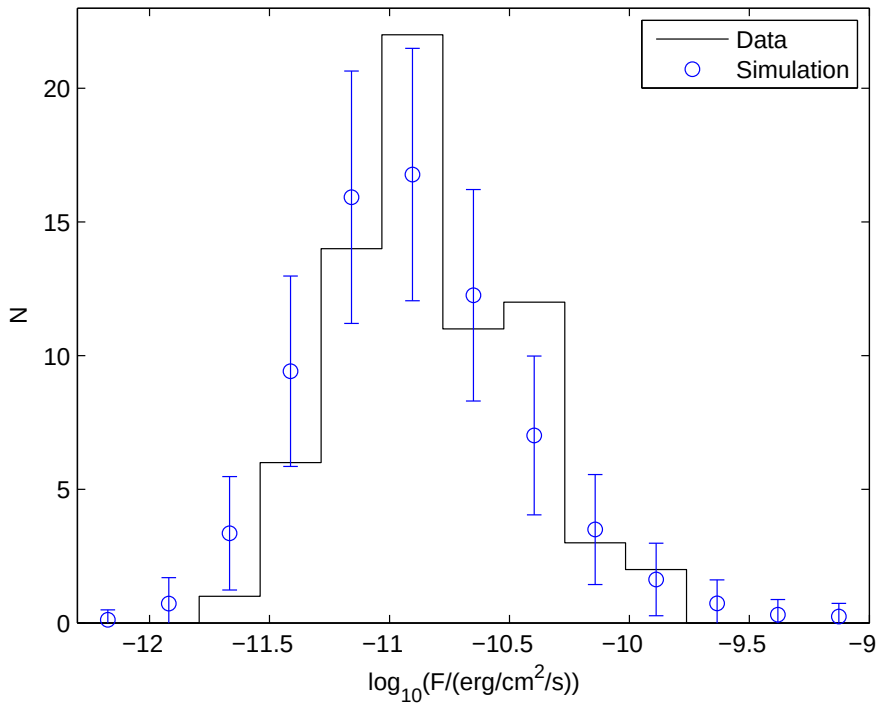

Figure 3.32: Simulated observed distribution of MSPs in flux for the simple power law luminosity distribution and X-shaped bulge model.

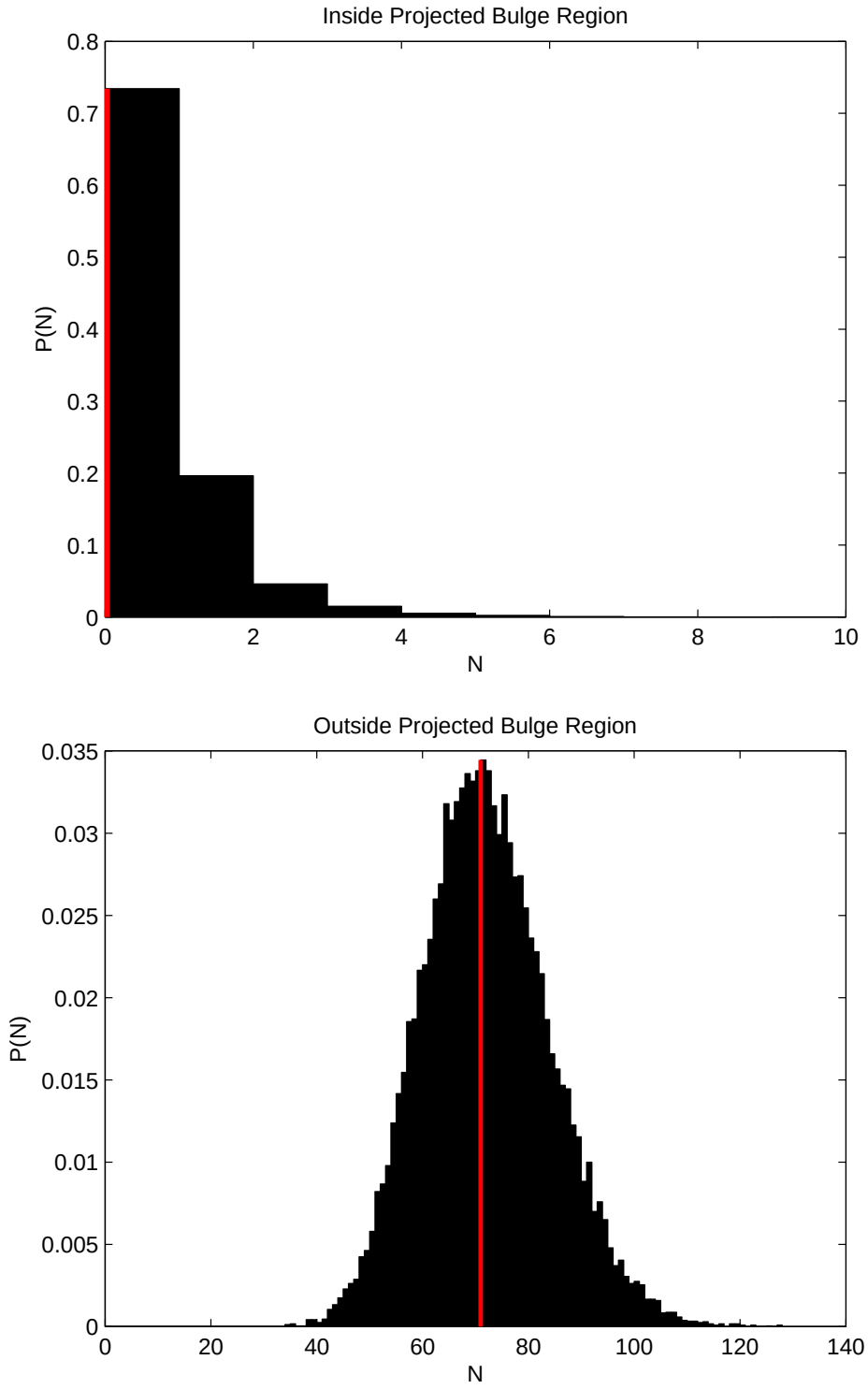

Figure 3.33: The approximate probability distributions of observing N MSPs inside and outside the projected bulge using the simple power law luminosity distribution and X-shaped bulge model. The red lines are the observed number for each case.

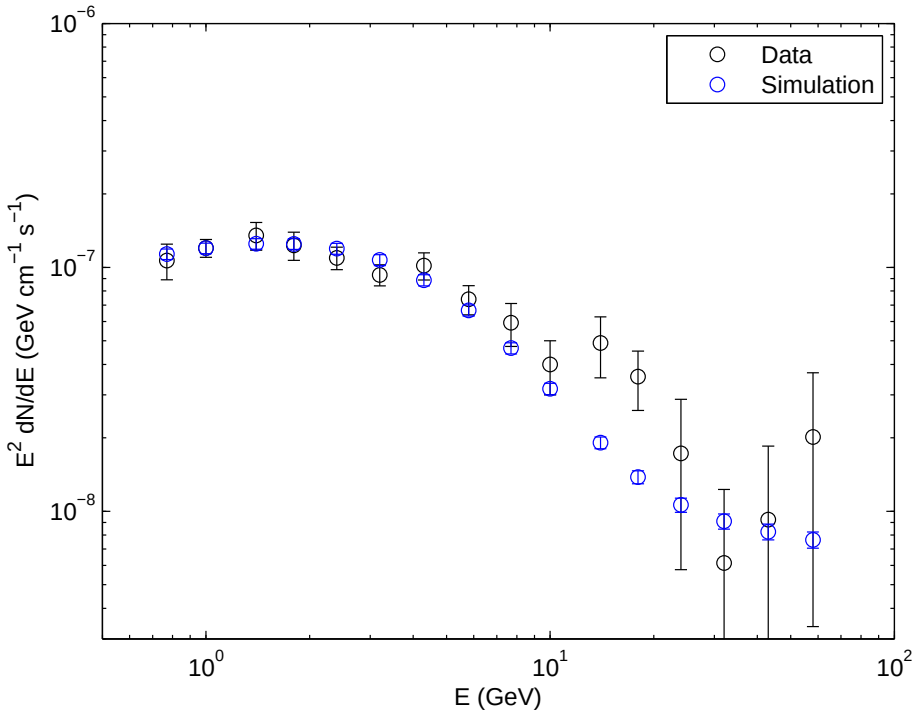

Figure 3.34: Simulated Galactic Center excess for the simple power law luminosity distribution and X-shaped bulge model.

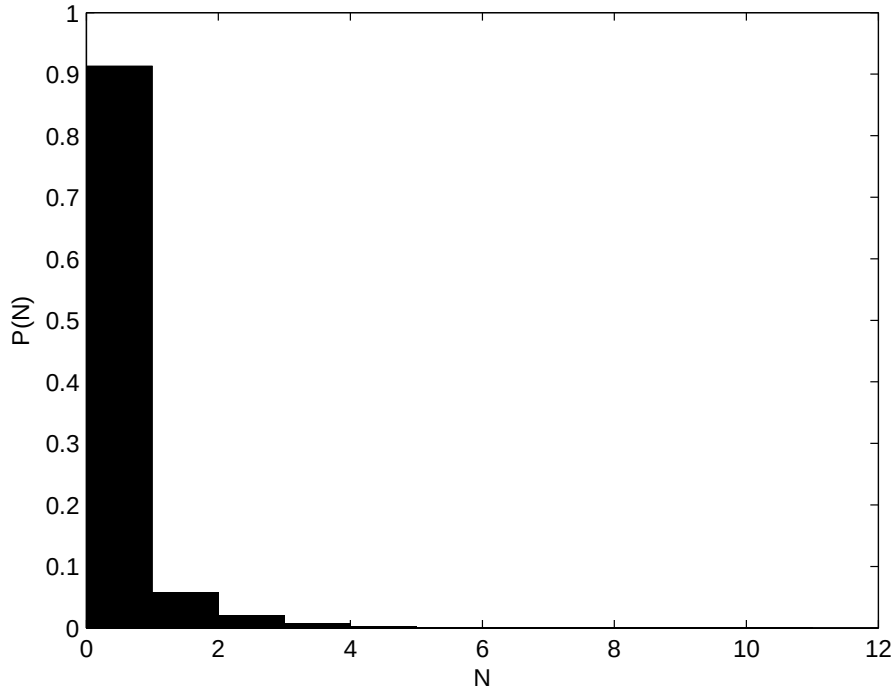

Figure 3.35: The probability distribution of observing N MSPs from the bulge population based on the simple power law luminosity distribution and X-shaped bulge model.

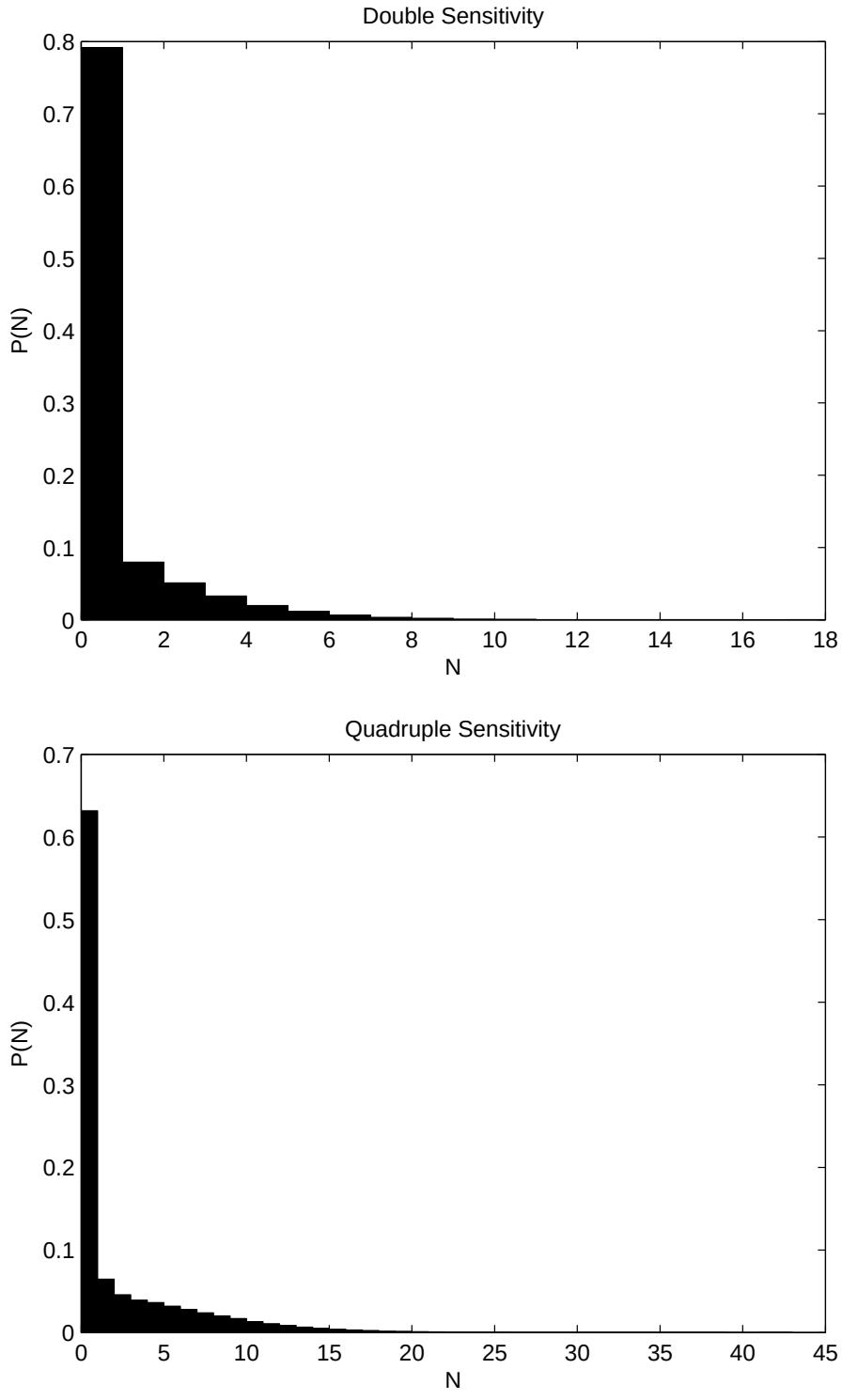

Figure 3.36: The probability distribution of observing N MSPs from the bulge population based on the simple power law luminosity distribution and X-shaped bulge model with double or quadruple sensitivity.

Chapter 4

Discussion

For each of the four models a set of figures are presented in Chapter 3 displaying simulated data produced using parameter sets in the Markov chains. The simulated distributions of resolved MSPs in longitude, latitude and flux are similar to those observed. The simulated GCE that could result from a population of MSPs in the galactic bulge generally fits the data well for both the spherically symmetric bulge and X-shaped bulge. Although only distances measured using parallax were included as priors on the distance parameters, the distance distributions of simulated resolved MSPs for all models are similar to that observed, including those distances estimated using the dispersion measure, but with a small downward shift. If, as the results suggest, the distances estimated using the dispersion measure tend to be overestimates, then this would also mean that MSP luminosities calculated using these distances (such as those in Abdo et al. [20]) have been overestimated. To estimate the size of this, for each d_i parameter and the distance measurement for the corresponding MSP $d_{\mathrm{data},i}$:

$$s_i = \frac{d_{\mathrm{data},i} - \bar{d}_i}{\bar{d}_i} \tag{4.1}$$

Then the mean s_i, excluding MSPs which did not have distance estimates, can be found for each model. Table 4.1 then shows that the distance measurements are on average around 50% higher than mean distances according to the model, or a shift of approximately 0.2 in $\log_{10}(d)$.

The simulated flux distribution requires the uncertain flux threshold to fit the data. When instead of F_{th} being drawn from a lognormal distribution, σ_{th} was removed as a parameter and the threshold was simply $\exp(\mu_{\mathrm{th}}(l,b) + K_{\mathrm{th}})$, the MCMC simulation produces Markov chains with parameters which predict a significantly larger number of resolved low flux MSPs and few higher flux MSPs, resulting in a

Model	$\bar{s_i}$
Lognormal with Spherical Bulge	0.53
Lognormal with X-shaped Bulge	0.35
Simple Power Law with Spherical Bulge	0.74
Simple Power Law with X-shaped Bulge	0.54

Table 4.1: Average relative difference s_i between mean model distance parameters and estimated distances to each MSP. Eq. 4.1 defines s_i.

poor fit to the flux distribution.

A significant difference between the spherically symmetric and X-shaped bulge models is the ratio $r_{\mathrm{d/b}}$. For both luminosity functions, the number of MSPs in the spherically symmetric bulge is similar to the number of disk MSPs. This is not the case when the X-shaped bulge model is used, here the number of disk MSPs is on average a factor of five larger, again for both luminosity functions. It can be seen that this difference is significant even when accounting for the uncertainties in the parameter $\ln\big(r_{\mathrm{d/b}}\big)$ by considering $|(\mu_1 - \mu_2)|/\sqrt{\sigma_1^2 + \sigma_2^2}$ where μ_1 and μ_2 are the means with errors σ_1 and σ_2 for each of the bulge models. This value is 2.47 for the lognormal luminosity function case, and in the case of the simple power law luminosity function it is 2.65.

In all four models for which results have been obtained using the MCMC algorithm, correlations are seen between $\ln\big(r_{\mathrm{d/b}}\big)$, K_{th} and σ_{th}. There are likely two causes for this, the first is that if K_{th} increases so must σ_{th}, if it does not the probability of observing an MSP with flux F_i, $p(F_i > F_{\mathrm{th,i}})$ in Eq. (2.38), drops for those MSPs where the measured flux is below the central flux threshold $\exp(\mu_{\mathrm{th}}(l_i, b_i) + K_{\mathrm{th}})$. The other cause of the correlation between the three variables is that if the flux threshold generally increases due to an increase in the parameter K_{th}, the number of MSPs must increase to compensate for the decrease in resolved MSPs. Combined with the fact that bulge MSPs are unlikely to be observed which means N_{bulge} is largely dependent on the GCE and the luminosity function, the increase occurs in N_{disk}, causing the parameter $r_{\mathrm{d/b}}$ to be higher. The correlation between $\ln\big(r_{\mathrm{d/b}}\big)$ and σ_{th} is then caused by the other two relationships.

The two models using the lognormal luminosity distribution also have a correlation between the two parameters $\log_{10}(L_{\mathrm{med}})$ and σ_L. This is because the observed data could be explained either by a large underlying population of MSPs with a broad distribution of luminosities and a median lower than those observed, or alternatively a smaller population of MSPs with a narrow luminosity distribution and

median luminosity similar to the observed MSPs. It is likely the luminosity distribution is also to some extent constrained by the distribution of resolved MSPs in the sky, for example, a broad luminosity function with a relatively high median would tend to produce distant resolved MSPs that would be clustered in the direction of the galactic center, this occurs not only because of the bulge model, but also because the peak density of the disk spatial model is there. On the other hand, a narrow luminosity function with a relatively low median would result in the distribution of resolved MSPs being more evenly distributed in the sky (except at low latitudes due to the higher flux threshold). This is a result of the fact that MSPs which pass the flux threshold test would tend to be nearby, and therefore would be found in a volume throughout which the density of MSPs is approximately constant.

A lower boundary of 31.0 was placed on the $\log_{10}(L_{\rm min})$ parameter for the simple power law luminosity function MCMC simulations. This was used due to the weak dependence of the likelihood on this parameter as it is reduced beyond this boundary. The cause of this is the improbability that an MSP with such low luminosities would be resolved, therefore if $L_{\rm min}$ is reduced, $N_{\rm disk}$ can simply be increased and the change in the predicted distribution of resolved MSPs is negligible. This also means, however, that $L_{\rm min}$ cannot actually be constrained using the observed MSP data, although the MCMC results do allow an upper limit to be placed on it, $\log_{10}(L_{\rm min}) < 31.8$ for both bulge models, largely due to that being the approximate log luminosity of the least luminous MSP with distance measured using parallax. For a similar reason, the distribution of $\log_{10}(L_{\rm max})$ is almost entirely above 33, which is the approximate log luminosity of the most luminous MSP. There is also a banana-shaped correlation between α and $\log_{10}(L_{\rm max})$. Where $\log_{10}(L_{\rm max})$ is lower, the MCMC algorithm explores a wide range of values for α, however as $\log_{10}(L_{\rm max})$ increases, α is increasingly restricted to higher values. This is simply because a high $\log_{10}(L_{\rm max})$ and lower α would result in a large number of resolved MSPs in the galactic center region.

Hooper and Mohlabeng [14] used the observed MSPs to attempt to find parameters for the lognormal luminosity function by using the product of three binned likelihoods in longitude, latitude and flux. In each bin the expected number of observations λ_i was found by taking a large number of random samples from the model, binning them and normalizing so that $\sum_{i=1}^{N} \lambda_i = 66$, where 66 was the number of MSPs used in the fit. The likelihood for each distribution was:

$$\mathcal{L} = \prod_i \frac{\lambda_i^{n_i} \exp(-\lambda_i)}{n_i!} \tag{4.2}$$

where n_i was the number of observed MSPs in bin i. The results are compared

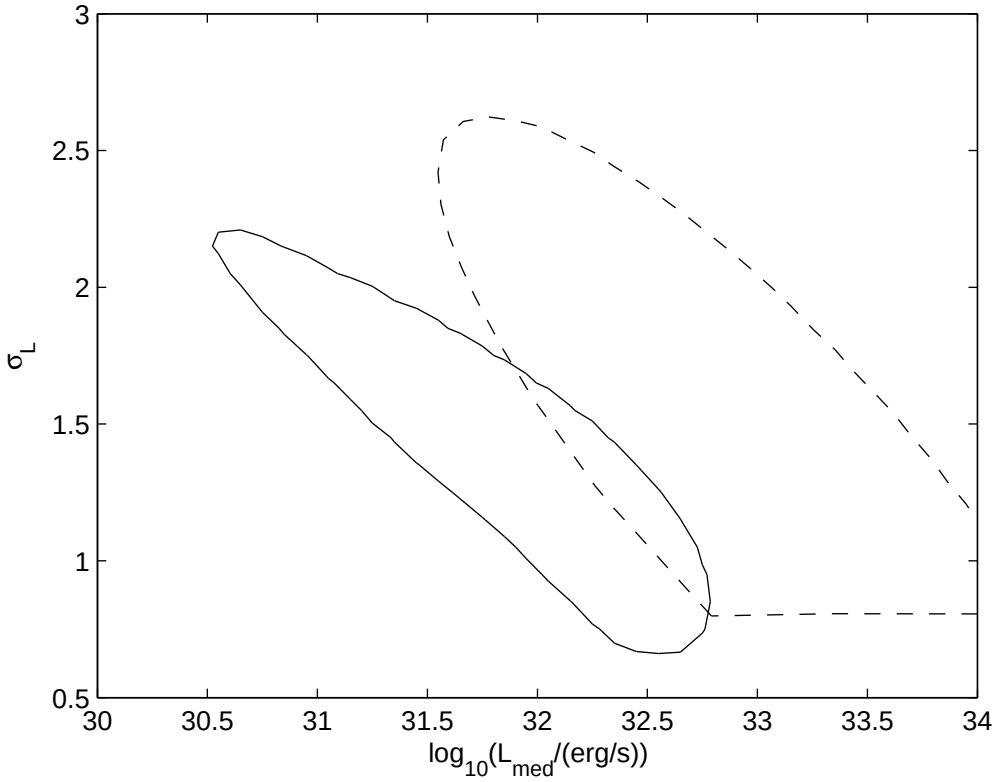

Figure 4.1: Contour plot of luminosity function parameter distribution showing the 95% contour for the lognormal luminosity distribution and spherical bulge model. The dashed line is the 2σ contour from [14].

to the results of this work for both the spherically symmetric and X-shaped bulge models in Figs. 4.1 and 4.2. While there is some agreement, the difference could be explained in part by the use of the parallax measured distances which were only used to estimate a lower bound on σ_L by Hooper and Mohlabeng [14]. The other significant difference between that study and this work is the form of likelihood used. Whereas Hooper and Mohlabeng [14] used the product of three likelihoods in each distribution longitude, latitude and flux, here these were not assumed to be separate. In addition the bulge model was included as part of the likelihood, not only to find parameters fitting the GCE, but also because some luminosity distributions could result in many observed bulge MSPs. This could reduce the likelihood for luminosity functions which tend to generate high luminosity MSPs with greater probability. It is also suggested by Hooper and Mohlabeng [14] that a further restriction can be placed on the luminosity function parameters by considering MSPs located in globular clusters. These were not taken into account here as it is not certain they would necessarily have the same luminosity distribution as the disk population.

It is concluded by Hooper and Mohlabeng [14] that many MSPs located in the

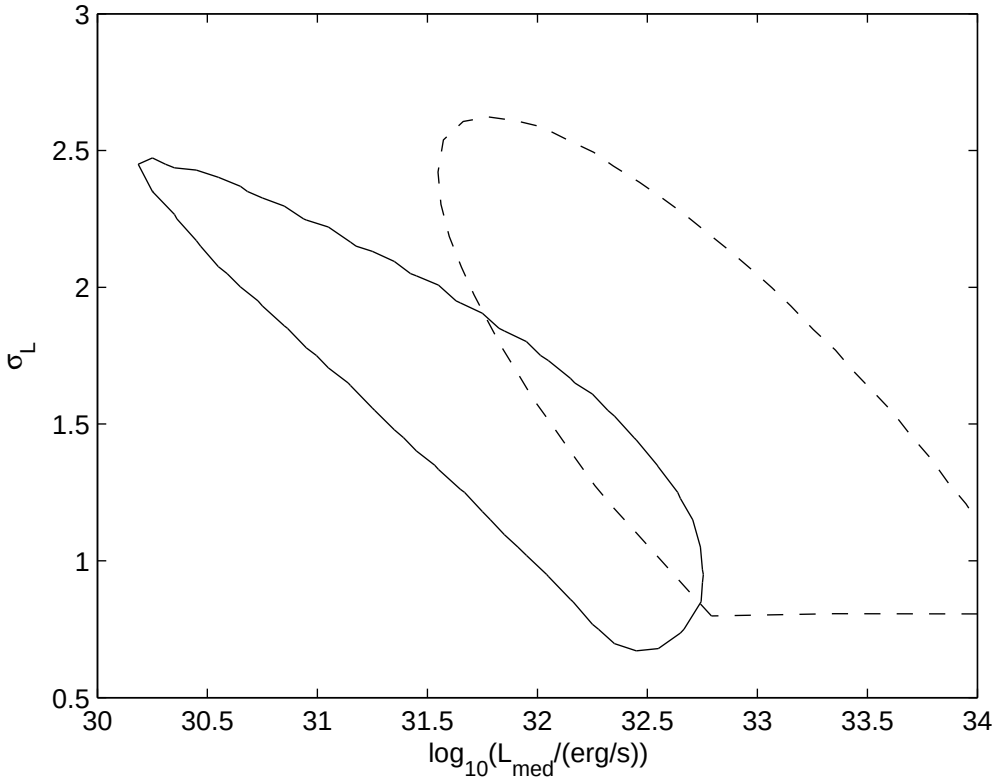

Figure 4.2: Contour plot of luminosity function parameter distribution showing the 95% contour for the lognormal luminosity distribution and X-shaped bulge model. The dashed line is the 2σ contour from [14].

bulge should have already been observed if the luminosity distribution is the same for disk and bulge MSPs. While the probability of observing bulge MSPs varies depending on the model used, in all cases the results of this work suggest it is unlikely that a bulge MSP would have been resolved based on the fitted threshold. Although six of the observed MSPs are inside the projected spherically symmetric bulge region of the sky, the distances estimated using dispersion measures indeed indicate that none are inside this bulge. No MSPs were observed in the region of the projected X-shaped bulge. With four times the current sensitivity to point sources it is likely, for all but the simple power law luminosity function with an X-shaped bulge model, that at least one bulge MSP could be resolved. In the case of the lognormal luminosity distribution with the spherical bulge model it is likely several would be resolved.

The lognormal distribution of luminosities could occur if surface magnetic field $B_{\rm S}$, period P and efficiency η all have lognormal distributions, where luminosity $L = \dot{E}\eta$. Using Eq. 1.2 and Eq. 1.4, the luminosity can then be found in terms of $B_{\rm S}$, P and η:

$$L = \frac{32\pi^4 R_{\rm NS}^6 B_{\rm S}^2 \eta}{3c^3 P^4} \tag{4.3}$$

Assuming $R_{\rm NS} = 10$, the luminosity distribution median can be written as [14]:

$$L_{\rm med} \approx 4.8 \times 10^{33} \left(\frac{B_{\rm S,med}}{10^{8.5}{\rm G}}\right)^2 \left(\frac{P_{\rm med}}{3{\rm ms}}\right)^{-4} \left(\frac{\eta_{\rm med}}{0.1}\right) \tag{4.4}$$

And, making the assumption that $B_{\rm S}$, P and η are not correlated, σ_L can be found from:

$$\begin{aligned} \sigma_L &= \sqrt{\left(\frac{\partial \ln(L)}{\partial \ln(P)}\right)^2 \sigma_P^2 + \left(\frac{\partial \ln(L)}{\partial \ln(B_{\rm S})}\right)^2 \sigma_B^2 + \left(\frac{\partial \ln(L)}{\partial \ln(\eta)}\right)^2 \sigma_\eta^2} \\ &= \sqrt{16\sigma_P^2 + 4\sigma_B^2 + \sigma_\eta^2} \end{aligned} \tag{4.5}$$

This differs from the incorrect $\sigma_L = 4\sigma_P + 2\sigma_B + \sigma_\eta$ given by Hooper and Mohlabeng [14]. If $P_{\rm med} = 4.9$ ms and $\sigma_P = 0.35$ as fitted in Hooper and Mohlabeng [14], if we assume $\eta_{\rm med} = 0.1$ and if, based on the results of the MCMC simulations for the two bulge models, $L_{\rm med} = 7 \times 10^{31}$ erg s^{-1}, then $B_{\rm S,med} \approx 10^8$ G which is similar to the ATNF catalog [21] MSPs as seen in the lower left of Fig. 1.4. This period distribution fit would also suggest that the luminosity function must be relatively broad, with $\sigma_L > 1.4$. However, correlations between $B_{\rm S}$, P and η may allow the luminosity distribution to be narrower.

A broken power law luminosity function, defined between 10^{32} erg s^{-1} and 10^{35} erg s^{-1}, was used by Yuan and Zhang [12]. This has the form:

$$p(L) \propto L^{-\alpha_1} \left(1 + \left(\frac{L}{L_{\rm br}}\right)^2\right)^{(\alpha_1 - \alpha_2)/2} \tag{4.6}$$

Using this luminosity model, a spherically symmetric bulge model with a 10° radius in the sky and the same disk model used in this work with spatial parameters $\sigma_r = 5$ kpc and $\sigma_z = 1$ kpc, it was shown that the observed data, including the lack of resolved MSPs from the bulge population, could be explained using the parameters listed in Table 4.2.

The simple power law is similar to the broken power law where $\alpha = \alpha_1$ and $L_{\rm max} = L_{\rm br}$ but with a large α_2. It can be seen then, in Figs. 3.19 and 3.28, that the results of the MCMC simulations for both bulge models are similar to those listed in Table 4.2.

α_1	α_2	$L_{\rm br}$ (10^{33} erg s^{-1})	$N_{\rm disk}$ ($L > 10^{32}$ erg s^{-1})	$N_{\rm bulge}$ ($L > 10^{32}$ erg s^{-1})
0.7	2.5	1.0	9000	17000
1.1	3.0	4.0	6000	13000
1.5	3.5	10.0	8000	16000

Table 4.2: Broken power law luminosity model parameters used by Yuan and Zhang [12]. $N_{\rm disk}$ and $N_{\rm bulge}$ are defined as the number of MSPs with luminosities above 10^{32} erg s^{-1}.

Chapter 5

Conclusion

A Markov chain Monte Carlo (MCMC) algorithm was used to constrain parameters for a set of models of the Milky Way millisecond pulsar (MSP) population, with the luminosity distribution being of particular interest. This was performed using the Galactic Center gamma-ray excess (GCE) data, the locations of observed MSPs in the sky, their fluxes and those distances where parallax distance measurements were available.

To confirm that the models could plausibly explain the observations, the Markov chains of parameters produced by the MCMC simulation were then used to produce simulated data. The simulated distributions of resolved MSPs were a good fit to the observed data, as were the simulations of the GCE.

These results indicate that it is possible that the source of the observed GCE could be an unresolved population of MSPs located around the Galactic Center with the same luminosity distribution as those observed. If this is indeed the case, based on these results, it could be expected that an improvement in the gamma-ray point source detection sensitivity by a factor of around four may allow a small number of MSPs from this population to be resolved. It was claimed by Hooper and Mohlabeng [14] that if the GCE was produced by MSPs, many of them would already have been resolved. Here, it has been shown that this is in fact not the case. The cause of this disagreement is likely due to Hooper and Mohlabeng [14] using an approximate likelihood to fit model parameters to the observed MSPs, and not including the parallax distance and GCE data in that fit.

In this work MSPs present in globular clusters were not included in finding constraints on the luminosity function parameters. Future work could involve incorporating these into the model. Two pulsars were also found in the 3FGL catalog which were associated with globular clusters, PSR J1823-3021A and PSR J1824-2452A. Both of these MSPs have unusually high $\dot{P}$ values which could indicate they

may be formed in some alternative process to typical MSPs [40], but this could also mean they do not have the same luminosity distribution.

Lee et al. [17] used a non-Poissonian template fit (NPTF) to show that the excess could be explained a population of unresolved point sources below the detection threshold. A similar conclusion is reached by Bartels et al. [18] using the wavelet transform of the Fermi Large Area Telescope gamma-ray data. Simulations of populations of MSPs with the fitted parameters of this work could be used to check for consistency with those results.

Bibliography

[1] L. Goodenough and D. Hooper, (2009), arXiv:0910.2998 [hep-ph].

[2] D. Hooper and T. Linden, Phys. Rev. **D84**, 123005 (2011), arXiv:1110.0006 [astro-ph.HE].

[3] K. N. Abazajian and M. Kaplinghat, Phys. Rev. **D86**, 083511 (2012), arXiv:1207.6047 [astro-ph.HE].

[4] C. Gordon and O. Macias, Phys. Rev. **D88**, [Erratum: Phys. Rev.D89,no.4,049901(2014)], 083521 (2013), arXiv:1306.5725 [astro-ph.HE].

[5] O. Macias and C. Gordon, Phys. Rev. **D89**, 063515 (2014), arXiv:1312.6671 [astro-ph.HE].

[6] K. N. Abazajian, N. Canac, S. Horiuchi, and M. Kaplinghat, Phys. Rev. **D90**, 023526 (2014), arXiv:1402.4090 [astro-ph.HE].

[7] T. Daylan, D. P. Finkbeiner, D. Hooper, T. Linden, S. K. N. Portillo, N. L. Rodd, and T. R. Slatyer, Phys. Dark Univ. **12**, 1–23 (2016), arXiv:1402.6703 [astro-ph.HE].

[8] F. Calore, I. Cholis, and C. Weniger, JCAP **3**, 038, 38 (2015), arXiv:1409.0042.

[9] M. Ajello et al., Astrophys. J. **819**, 44 (2016), arXiv:1511.02938 [astro-ph.HE].

[10] R.-Z. Yang and F. Aharonian, Astron. & Astrophys. **589**, A117, A117 (2016), arXiv:1602.06764 [astro-ph.HE].

[11] O. Macias, C. Gordon, R. M. Crocker, B. Coleman, D. Paterson, S. Horiuchi, and M. Pohl, (2016), arXiv:1611.06644 [astro-ph.HE].

[12] Q. Yuan and B. Zhang, JHEAp **3-4**, 1–8 (2014), arXiv:1404.2318 [astro-ph.HE].

[13] R. M. O'Leary, M. D. Kistler, M. Kerr, and J. Dexter, (2015), arXiv:1504.02477 [astro-ph.HE].

[14] D. Hooper and G. Mohlabeng, JCAP **1603**, 049 (2016), arXiv:1512.04966 [astro-ph.HE].

[15] I. Cholis, D. Hooper, and T. Linden, JCAP **1506**, 043 (2015), arXiv:1407.5625 [astro-ph.HE].

[16] D. Hooper, I. Cholis, T. Linden, J. Siegal-Gaskins, and T. Slatyer, Phys. Rev. **D88**, 083009 (2013), arXiv:1305.0830 [astro-ph.HE].

[17] S. K. Lee, M. Lisanti, B. R. Safdi, T. R. Slatyer, and W. Xue, Phys. Rev. Lett. **116**, 051103, 051103 (2016), arXiv:1506.05124 [astro-ph.HE].

[18] R. Bartels, S. Krishnamurthy, and C. Weniger, Phys. Rev. Lett. **116**, 051102, 051102 (2016), arXiv:1506.05104 [astro-ph.HE].

[19] S. Horiuchi, M. Kaplinghat, and A. Kwa, JCAP **1611**, 053 (2016), arXiv:1604.01402 [astro-ph.HE].

[20] A. A. Abdo et al., Astrophys. J. Suppl. **208**, 17 (2013), arXiv:1305.4385 [astro-ph.HE].

[21] R. N. Manchester, G. B. Hobbs, A Teoh, and M Hobbs, Astron. J. **129**, 1993 (2005), arXiv:astro-ph/0412641 [astro-ph].

[22] A. A. Abdo, M. Ackermann, M. Ajello, W. B. Atwood, M. Axelsson, L. Baldini, J. Ballet, G. Barbiellini, M. G. Baring, D. Bastieri, and et al., Astrophys. J. Suppl. **187**, 460–494 (2010), arXiv:0910.1608 [astro-ph.HE].

[23] J. M. Lattimer and M. Prakash, Science **304**, 536–542 (2004), arXiv:astro-ph/0405262 [astro-ph].

[24] D. R. Lorimer, Living Rev. Rel. **11**, 8 (2008), arXiv:0811.0762 [astro-ph].

[25] J. M. Cordes and T. J. W. Lazio, (2002), arXiv:astro-ph/0207156 [astro-ph].

[26] H. Heiselberg and V. Pandharipande, Ann. Rev. Nucl. Part. Sci. **50**, 481–524 (2000), arXiv:astro-ph/0003276 [astro-ph].

[27] A. Y. Potekhin, Physics Uspekhi **53**, 1235–1256 (2010), arXiv:1102.5735 [astro-ph.SR].

[28] M. A. Alpar, A. F. Cheng, M. A. Ruderman, and J. Shaham, Nature **300**, 728–730 (1982).

[29] T. M. Tauris, N. Langer, and M. Kramer, Mon. Not. R. Astron. So **425**, 1601–1627 (2012), arXiv:1206.1862 [astro-ph.SR].

[30] I. A. Grenier and A. K. Harding, Comptes Rendus Physique **16**, 641–660 (2015), arXiv:1509.08823 [astro-ph.HE].

[31] F. Acero et al., Astrophys. J. Suppl. **218**, 23 (2015), arXiv:1501.02003 [astro-ph.HE].

[32] W. Press, S. Teukolsky, W. Vetterling, and B. Flannery, *Numerical Recipes in C*, 2nd ed. (Cambridge University Press, United States of America, 1992).

[33] A. Gelman, J. Carlin, H. Stern, D. Dunson, A. Vehtari, and D. Rubin, *Bayesian Data Analysis*, 3rd ed. (CRC Press, United States of America, 2013).

[34] H. Haario, E. Saksman, and J. Tamminen, Bernoulli **7**, 223–242 (2001).

[35] W. Cash, Astrophys. J. **228**, 939–947 (1979).

[36] C.-A. Faucher-Giguère and A. Loeb, JCAP **1**, 005 (2010), arXiv:0904.3102 [astro-ph.HE].

[37] T. Grégoire and J. Knödlseder, Astron. Astrophys. **554**, A62 (2013), arXiv:1305.1584 [astro-ph.GA].

[38] S. A. Story, P. L. Gonthier, and A. K. Harding, Astrophys. J. **671**, 713–726 (2007), arXiv:0706.3041 [astro-ph].

[39] D. Foreman-Mackey, The Journal of Open Source Software **24** (2016) 10.21105/joss.00024.

[40] T. J. Johnson et al., Astrophys. J. **778**, 106 (2013), arXiv:1310.1852 [astro-ph.HE].

Appendix A

Data

E (GeV)	dN/dE (GeV^{-1} cm^{-2} s^{-1})
0.46	$(1.0 \pm 0.3) \times 10^{-6}$
0.62	$(5 \pm 2) \times 10^{-7}$
0.84	$(3.2 \pm 0.9) \times 10^{-7}$
1.1	$(2.0 \pm 0.5) \times 10^{-7}$
1.5	$(1.4 \pm 0.3) \times 10^{-7}$
2.0	$(6 \pm 1) \times 10^{-8}$
2.7	$(3.7 \pm 0.6) \times 10^{-8}$
3.6	$(1.6 \pm 0.3) \times 10^{-8}$
4.8	$(5 \pm 1) \times 10^{-9}$
6.5	$(3.5 \pm 0.7) \times 10^{-9}$
8.6	$(1.2 \pm 0.3) \times 10^{-9}$

Table A.1: Galactic Center gamma-ray excess data for spherically symmetric bulge model. Data from [4].

E (GeV)	dN/dE (GeV^{-1} cm^{-2} s^{-1})
0.77	$(1.8 \pm 0.3) \times 10^{-7}$
1.0	$(1.2 \pm 0.1) \times 10^{-7}$
1.4	$(6.9 \pm 0.9) \times 10^{-8}$
1.8	$(3.8 \pm 0.5) \times 10^{-8}$
2.4	$(1.9 \pm 0.2) \times 10^{-8}$
3.2	$(9.1 \pm 0.9) \times 10^{-9}$
4.3	$(5.5 \pm 0.7) \times 10^{-9}$
5.8	$(2.2 \pm 0.3) \times 10^{-9}$
7.7	$(1.0 \pm 0.2) \times 10^{-9}$
10	$(4 \pm 1) \times 10^{-10}$
14	$(2.5 \pm 0.7) \times 10^{-10}$
18	$(1.1 \pm 0.3) \times 10^{-10}$
24	$(3 \pm 2) \times 10^{-11}$
32	$(6 \pm 6) \times 10^{-12}$
43	$(5 \pm 5) \times 10^{-12}$
58	$(6 \pm 5) \times 10^{-12}$

Table A.2: Galactic Center gamma-ray excess data for X-shaped bulge model. Data from [11].

Name	l (deg)	b (deg)	Flux (10^{-11} erg cm^{-2} s^{-1})	Γ (or α)	$E_{\rm cut}$ (GeV)	β	E_0 (GeV)	d (kpc)
J0023+0923	111.5	-52.9	0.73 ± 0.08	1.0 ± 0.3	1.0 ± 0.2	-	0.90	0.7 ± 0.1
J0030+0451	113.1	-57.6	6.1 ± 0.2	1.28 ± 0.05	2.1 ± 0.2	-	0.76	$0.28^{+0.1}_{-0.06}$ (P)
J0034-0534	111.5	-68.1	1.8 ± 0.1	1.7 ± 0.1	2.9 ± 0.6	-	0.70	0.5 ± 0.1
J0101-6422	301.2	-52.7	1.25 ± 0.09	1.5 ± 0.1	2.9 ± 0.6	-	0.90	$0.55^{+0.09}_{-0.08}$
J0102+4839	124.9	-14.2	1.7 ± 0.1	1.8 ± 0.1	6 ± 2	-	1.2	$2.3^{+0.5}_{-0.4}$
J0218+4232	139.5	-17.5	4.8 ± 0.2	1.94 ± 0.06	4.7 ± 0.8	-	0.74	$2.7^{+1.1}_{-0.7}$
J0251+26	153.9	-29.5	0.7 ± 0.1	2.3 ± 0.1	-	-	1.1	$0.8^{+0.2}_{-0.1}$
J0307+7443	131.7	14.2	1.46 ± 0.08	0.5	1.24 ± 0.07	-	1.9	-
J0340+4130	153.8	-11.0	2.2 ± 0.1	1.3 ± 0.1	3.8 ± 0.7	-	1.4	1.7 ± 0.3
J0437-4715	253.4	-42.0	1.79 ± 0.09	1.3 ± 0.1	1.0 ± 0.2	-	0.59	0.156 ± 0.001 (P)
J0533+6759	144.8	18.2	0.96 ± 0.09	1.6 ± 0.2	6 ± 2	-	1.4	$2.4^{+0.9}_{-0.6}$
J0605+3757	174.2	8.0	0.7 ± 0.1	0.7 ± 0.4	1.5 ± 0.4	-	1.5	0.7 ± 0.1
J0610-2100	227.7	-18.2	1.1 ± 0.1	2.34 ± 0.07	-	-	0.85	-

Name	l (deg)	b (deg)	Flux (10^{-11} erg cm^{-2} s^{-1})	Γ (or α)	$E_{\rm cut}$ (GeV)	β	E_0 (GeV)	d (kpc)
J0613-0200	210.4	-9.3	3.4 ± 0.2	1.4 ± 0.1	2.9 ± 0.4	-	1.1	$0.9^{+0.4}_{-0.2}$ (P)
J0614-3329	240.5	-21.8	11.1 ± 0.2	1.36 ± 0.03	4.7 ± 0.3	-	0.88	1.9 ± 0.4
J0621+2514	187.1	5.1	1.1 ± 0.1	2.17 ± 0.09	-	-	1.7	$2.3^{+0.5}_{-0.4}$
J0751+1807	202.8	21.1	1.3 ± 0.1	1.3 ± 0.2	3.0 ± 0.6	-	1.2	$0.4^{+0.2}_{-0.1}$ (P)
J0931-1902	251.0	23.0	0.30 ± 0.09	1.8 ± 0.2	-	-	3.4	$1.9^{+0.5}_{-0.4}$
J0955-61	283.7	-5.7	0.8 ± 0.1	2.3 ± 0.1	-	-	1.2	$4.0^{+0.9}_{-0.8}$
J1024-0719	251.7	40.5	0.36 ± 0.05	0.5	1.4 ± 0.2	-	2.1	0.39 ± 0.04
J1124-3653	284.1	22.8	1.3 ± 0.1	1.3 ± 0.2	3.1 ± 0.7	-	1.4	1.7 ± 0.4
J1125-5825	291.8	2.6	1.5 ± 0.3	2.4 ± 0.1	-	-	1.9	2.6 ± 0.4
J1125-6014	292.5	0.9	1.2 ± 0.3	2.4 ± 0.1	-	-	2.1	1.5 ± 0.2
J1137+7528	129.1	40.8	0.23 ± 0.06	2.3 ± 0.2	-	-	1.5	-
J1142+0119	267.6	59.4	0.62 ± 0.08	1.2 ± 0.3	5 ± 2	-	1.8	0.9 ± 0.2
J1207-5050	295.9	11.4	0.8 ± 0.1	2.1 ± 0.1	-	-	1.5	1.5 ± 0.2

Name	l (deg)	b (deg)	Flux (10^{-11} erg cm^{-2} s^{-1})	Γ (or α)	$E_{\rm cut}$ (GeV)	β	E_0 (GeV)	d (kpc)
J1227-4853	299.0	13.8	4.1 ± 0.2	2.23 ± 0.05	-	0.11 ± 0.03	0.44	1.4 ± 0.2
J1231-1411	295.5	48.4	10.3 ± 0.2	1.18 ± 0.04	2.6 ± 0.2	-	0.92	0.44 ± 0.05
J1301+0833	310.8	71.3	1.1 ± 0.1	2.4 ± 0.1	-	-	0.77	0.7 ± 0.1
J1302-3258	305.6	29.8	1.1 ± 0.1	1.1 ± 0.2	2.7 ± 0.7	-	1.4	1.0 ± 0.2
J1311-3430	307.7	28.2	6.5 ± 0.2	1.91 ± 0.05	5.1 ± 0.8	-	0.66	1.4 ± 0.3
J1312+0051	314.8	63.2	1.6 ± 0.1	1.5 ± 0.1	2.8 ± 0.6	-	0.84	$0.8 \pm ^{+0.2}_{-0.1}$
J1400-1438	326.9	45.0	0.9 ± 0.1	2.30 ± 0.08	-	-	0.95	0.48 ± 0.03
J1446-4701	322.5	11.4	1.3 ± 0.1	2.30 ± 0.08	-	-	1.0	1.5 ± 0.2
J1514-4946	325.2	6.8	4.3 ± 0.2	1.43 ± 0.09	5.0 ± 0.7	-	1.5	0.9 ± 0.1
J1536-4948	328.2	4.8	8.7 ± 0.3	1.87 ± 0.03	-	0.17 ± 0.02	1.0	1.8 ± 0.1
J1543-5149	327.9	2.7	2.2 ± 0.3	2.5 ± 0.1	-	-	0.83	2.4 ± 0.2
J1544+4937	79.2	50.2	0.36 ± 0.06	2.3 ± 0.1	-	-	1.1	$1.2^{+0.4}_{-0.3}$
J1600-3053	344.1	16.5	0.6 ± 0.1	1.0 ± 0.5	3 ± 2	-	2.6	1.6 ± 0.3

Name	l (deg)	b (deg)	Flux (10^{-11} erg cm^{-2} s^{-1})	Γ (or α)	$E_{\rm cut}$ (GeV)	β	E_0 (GeV)	d (kpc)
J1614-2230	352.6	20.2	2.3 ± 0.1	0.8 ± 0.2	1.8 ± 0.3	-	1.4	0.65 ± 0.05 (P)
J1628-3205	347.4	11.5	1.2 ± 0.1	2.3 ± 0.1	-	0.4 ± 0.1	1.0	1.3 ± 0.2
J1630+3734	60.2	43.3	0.7 ± 0.1	1.0 ± 0.4	2.0 ± 0.6	-	1.6	0.9 ± 0.1
J1658-5324	334.9	-6.6	2.0 ± 0.2	1.4 ± 0.2	1.4 ± 0.3	-	1.0	0.9 ± 0.1
J1713+0747	28.8	25.2	0.9 ± 0.1	1.4 ± 0.3	3 ± 1	-	1.4	$1.05^{+0.06}_{-0.05}$
J1732-5049	340.0	-9.4	0.9 ± 0.1	2.4 ± 0.1	-	-	0.96	1.4 ± 0.2
J1741+1351	37.9	21.6	0.6 ± 0.1	2.2 ± 0.1	-	-	1.3	$1.08^{+0.04}_{-0.05}$ (P)
J1744-1134	14.8	9.2	3.9 ± 0.2	1.4 ± 0.1	1.5 ± 0.2	-	0.75	0.42 ± 0.02 (P)
J1745+1017	34.9	19.3	1.1 ± 0.1	1.5 ± 0.3	4 ± 1	-	1.5	$1.3^{+0.2}_{-0.1}$
J1747-4036	350.2	-6.4	1.6 ± 0.2	2.3 ± 0.1	-	-	1.2	3.4 ± 0.8
J1805+06	33.4	13.0	0.5 ± 0.1	1.7 ± 0.3	-	0.6 ± 0.2	1.9	$2.5^{+0.5}_{-0.4}$
J1810+1744	44.6	16.8	2.2 ± 0.1	1.8 ± 0.1	2.9 ± 0.7	-	0.66	$2.0^{+0.3}_{-0.2}$
J1816+4510	72.9	24.8	1.21 ± 0.09	1.7 ± 0.1	5 ± 1	-	0.91	$2.4^{+0.7}_{-0.4}$

Name	l (deg)	b (deg)	Flux (10^{-11} erg cm^{-2} s^{-1})	Γ (or α)	$E_{\rm cut}$ (GeV)	β	E_0 (GeV)	d (kpc)
J1843-1113	22.0	-3.4	2.0 ± 0.3	2.7 ± 0.1	-	-	0.50	1.7 ± 0.2
J1858-2216	13.6	-11.4	0.8 ± 0.1	0.7 ± 0.4	1.8 ± 0.6	-	1.6	0.9 ± 0.1
J1902-5105	345.6	-22.4	2.1 ± 0.1	1.8 ± 0.1	3.5 ± 0.9	-	0.62	1.2 ± 0.2
J1903-7051	324.4	-26.5	1.2 ± 0.1	2.32 ± 0.07	-	-	0.91	0.8 ± 0.1
J1959+2048	59.2	-4.7	1.8 ± 0.2	1.3 ± 0.2	1.4 ± 0.3	-	0.80	$2.5^{+0.2}_{-0.5}$
J2017+0603	48.6	-16.0	3.5 ± 0.2	1.1 ± 0.1	3.7 ± 0.5	-	1.7	1.6 ± 0.2
J2042+0246	49.0	-23.0	0.36 ± 0.06	2.3 ± 0.3	-	1	1.2	-
J2043+1711	61.9	-15.3	3.0 ± 0.1	1.58 ± 0.08	4.5 ± 0.8	-	0.96	$1.8^{+0.1}_{-0.3}$
J2047+1053	57.1	-19.6	0.36 ± 0.06	0.5	1.7 ± 0.3	-	2.6	2.1 ± 0.3
J2051-0827	39.2	-30.5	0.32 ± 0.05	0.5	1.6 ± 0.3	-	2.4	$1.0^{+0.2}_{-0.1}$
J2124-3358	10.9	-45.4	3.9 ± 0.1	0.9 ± 0.1	1.9 ± 0.2	-	1.1	$0.30^{+0.07}_{-0.05}$ (P)
J2129-0429	48.9	-36.9	1.0 ± 0.1	2.22 ± 0.07	-	-	1.0	0.9 ± 0.1
J2214+3000	86.9	-21.7	3.3 ± 0.1	1.20 ± 0.08	2.4 ± 0.3	-	0.94	1.5 ± 0.2

Name	l (deg)	b (deg)	Flux (10^{-11} erg cm^{-2} s^{-1})	Γ (or α)	$E_{\rm cut}$ (GeV)	β	E_0 (GeV)	d (kpc)
J2215+5135	99.9	-4.2	1.4 ± 0.1	1.4 ± 0.2	3.5 ± 0.8	-	1.3	$3.0^{+0.3}_{-0.4}$
J2234+0944	76.3	-40.4	0.8 ± 0.1	1.3 ± 0.3	2.1 ± 0.7	-	1.1	-
J2241-5236	337.4	-54.9	3.1 ± 0.1	1.25 ± 0.08	2.8 ± 0.4	-	0.94	0.51 ± 0.08
J2256-1024	59.2	-58.2	0.77 ± 0.08	1.2 ± 0.2	2.3 ± 0.6	-	1.2	0.6 ± 0.1
J2302+4442	103.4	-14.0	3.8 ± 0.1	1.19 ± 0.08	3.0 ± 0.3	-	1.1	$1.2^{+0.1}_{-0.2}$
J2339-0533	81.3	-62.5	3.0 ± 0.1	1.51 ± 0.08	5.1 ± 0.9	-	0.96	-

Table A.3: List of observed millisecond pulsars. For the spectral parameters, MSPs with neither the $E_{\rm cut}$ or β columns filled have been fitted with a simple power law spectrum, those with $E_{\rm cut}$ filled have been fitted with an exponentially cutoff power law, and those with the β column filled have been fitted with a log parabolic spectrum. Data from 3FGL catalog [31] except distance measurements. A (P) in the distance column indicates the distance is that reported in [20] and was found using the parallax method. Other distances were derived from the dispersion measure reported in the ATNF pulsar catalog [21] using the NE2001 model [25].